Treball de Fi de Grau

Study of Alternative Geometries for Fluidic Oscillators by means of Computational Fluid Mechanics

Report

Author:
Xavier Baucells Fuster

Director:
David del Campo Sud
Co-Director:
Vanessa del Campo Gatell

Grau en Enginyeria en Tecnologies Aeroespacials

in

Escola Tècnica Superior d'Enginyeries Industrial i Aeronàutica de Terrassa

ETSEIAT - UPC

June, 12th of 2015

Contents

List of Figures

List of Tables

Chapter 1

Introduction

1.1 Aim

A 2D study will be carried out regarding the flux of a fluid through a fluidic oscillator by means of a Computational Fluid Mechanics commercial code. The results will be compared with previous experimental analysis made by Raghu et al. [1]. This will provide more data for further investigations of the geometry used. The fluidic oscillator studied in the present work is shown in figure 1.1.

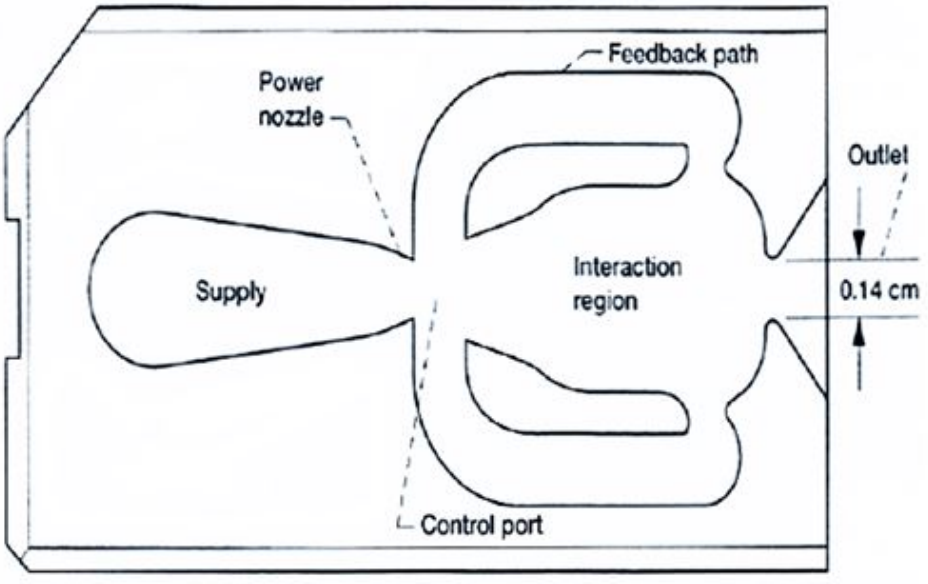

FIGURE 1.1: Fluidic oscillator studied by Raghu et al. [1]

1.2 Scope

The study of the chosen fluidic oscillator comprises many stages. On the first place, an introductory section defines a general background for the study. This section contains the state of the art analysis and the principles in which fluidic oscillators are based. Moreover, in regards of the aeronautical applications of the oscillators in which this work is focused, a revision of the fundamental concepts related to the boundary layer separation, drag and the stall of a wing is also made. Finally, the current competitors for aeronautical applications are also analysed.

The next section starts with a review of 2 significant studies for the present work. Those studies are made by Ruiz [8] and Raghu et al. [1]. The first study is important because it constitutes the previous research done in Escola Tècnica Superior d'Enginyeries Industrial i Aeronàutica de Terrassa (ETSEIAT), in Universitat Politècnica de Catalunya (UPC), in the line of investigation on fluidic oscillators, and it provides essential information for the numerical study, such as the best model for the simulation: the turbulence SST model. The second work is a paper about an experimental study on the use of fluidic oscillators in thrust vectoring. It contains information about frequency range vs inlet gauge pressure of the fluidic oscillator that is studied in the present work. According to the paper, the fluid of study is air, having as boundary conditions both the inlet and the outlet pressure: a range between 10 and 165.47 kPa for the inlet and ambient pressure for the outlet. However, the data provided in the paper by Raghu et al. [1] is incomplete, and it is possible that the image of the oscillator provided does not exactly correspond to the real geometry tested by Raghu and be slightly distorted in some way. This needs to be considered as well in the final results.

Having said that, the next step consists in a CAD reproduction of the image of the oscillator and its correctly meshing with ICEM-CFD. Then, the boundary conditions and the solution methods must be set with ANSYS-Fluent, continuing with the solution calculation and a final analysis of the results, which must be validated with the information provided by Raghu et al. [1]. The experimental frequency range obtained by Raghu was 400-1600 Hz for the different inlet pressure levels. Moreover, the flow main characteristics must be identified.

In order to achieve the goals of the study, there is a set of tasks that must be fulfilled. Among those, some correspond to the learning of the possibilities and fundamentals of the programmes used, while the others consist directly in the study of the element.

- State of the art and general background research: Previous investigation of fluidic oscillators and the theoretical aspects involved must be learned.

- CAD drawings of the fluidic oscillator geometry: Starting with an image of the fluidic oscillator studied by Raghu et al. [1], a reproduction has to be drawn with CAD tools.

- Meshing fundamentals' learning: The absence of previous experience in meshing requires the dedication of a significant amount of time to its fundamental aspects' learning, and some experience gathering with simple examples.

- Geometry meshing: A precise and efficient mesh must be designed. Two main aspects must be considered: maximum precision and minimum computing cost, so that a balanced mesh can be found.

- CFD fundamentals and ANSYS-FLUENT learning: The theoretical background of the CFD calculations must be understood. In addition, the software utilisation must be learned so that its capabilities are fully exploited.

- CFD simulation: Setting the conditions of the simulation and running the analysis. Many simulations of the different meshes used will be carried out during the development of the project.

- Results analysis: A post-process must be applied to the data collected from the CFD simulation in order to obtain the performance parameters of the oscillator. The results must also be compared with experimental data provided by Raghu et al. [1].

Table 1.1 shows the time estimation to dedicate to each task and table 1.2 the dependencies between them (the preparation of the draft and its revision are also time consuming so they have been included in the tasks' organisation below).

Code	Task	Time dedication [hours]
TBR	State of the art and general background research	30
CAD	CAD drawings of the fluidic oscillator geometry	10
MF	Meshing fundamentals' learning	30
GM	Geometry meshing	100
CFD-L	CFD fundamentals and software learning	20
CFD-S	CFD simulation	100
RA	Results analysis	30
DP	Draft preparation	60
RV	Revision	10
	Total	**380**

Table 1.1: Time estimation

Code	Task	Preceding task
TBR	State of the art and working principles research	-
CAD	CAD drawings of the fluidic oscillator geometry	-
MF	Meshing fundamentals' learning	-
GM	Geometry meshing	MF
CFD-L	CFD fundamentals and software learning	-
CFD-S	CFD simulation	CFD-L, GM
RA	Results analysis	CFD-S
DP	Draft preparation	-
RV	Revision	DP

TABLE 1.2: Dependencies between tasks

Finally, a Gantt Chart is provided in figure 1.2 in order to illustrate the overall work distribution.

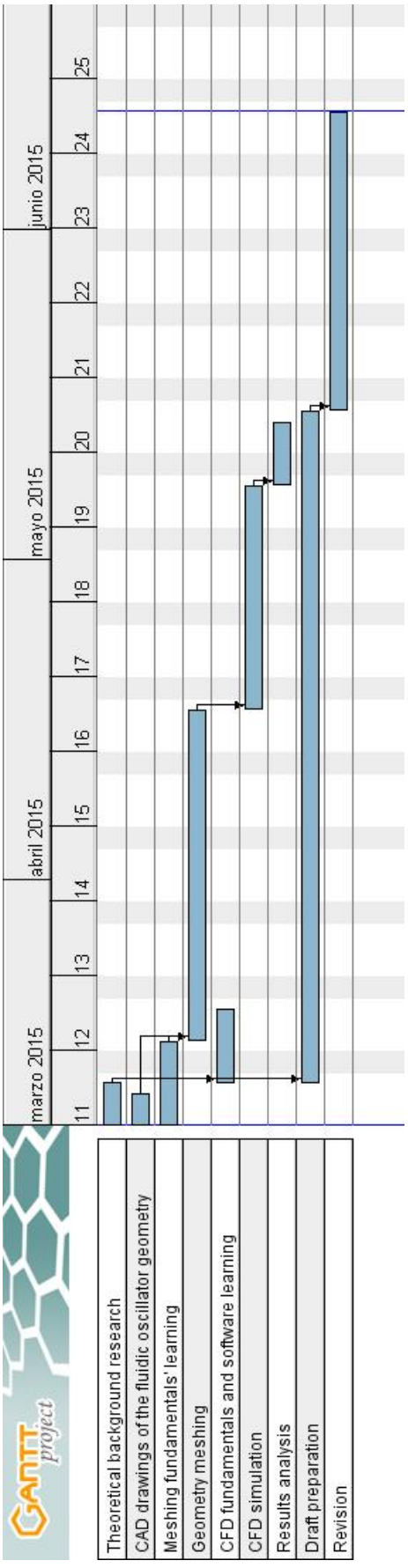

FIGURE 1.2: Gantt Chart planning

1.3 Requirements

As the project is focused on the study of an already defined device, all of its characteristics and performances are also pre-defined, given that the design process is not considered here. However, the performance of the device is not the single requirement of a study. On the first place, the geometry has to be as similar as possible to the one provided in the paper by Raghu et al. [1]. The data provided in this paper is incomplete and not always clear (the geometry shown in the paper could even be slightly distorted with respect to the real one), so this might lead to disagreement of the results. On the second place, the conditions of the simulation must be, as far as possible, the same as the ones used in the experimental analysis and the final results should also be similar to the ones obtained experimentally. This experimental data has been introduced in the Scope section and is detailed in chapter 4. Finally, the analysis should also include the flow characterisation, which means that the main characteristics of the flow must be identified.

Apart from that, the study must contain an introductory section that establishes a sufficient background. Moreover, the numerical analysis requires the use of a good and fine enough mesh, while at the same time, the computing cost should not be excessive in terms of time dedication, so a good balance must be achieved.

1.4 Justification

Boundary layer control is one of the major investigation paths in the aeronautical field due to its relevance for flow separation. When the boundary layer loses enough energy, it may no longer follow an obstacle shape (a wing generally) and thus no lift is generated and the drag is significantly increased. This is also important in non-aeronautical cases. For example, the boundary layer separation in blunt bodies such as transportation vehicles is responsible for their high drag.

Fluidic oscillators can provide a solution for the boundary layer control: they are carefully designed so that the emergent flow sweeps with a specific controlled frequency, energizing the boundary layer and thus providing the required control. Besides, a fluidic oscillator is a simple and small device that has no moving parts [14, 15]. In addition, there are many other applications, such as turbulent mixing enhancement for combustion [16] or thrust vectoring [1]. All these processes can be carried out with extremely low mass flow rates, resulting in an almost non-consuming or even totally non-consuming technology, that enables considerable efficiency increases and drastic energy consumption reduction in all kinds of vehicles [15]. Moreover, it is important to highlight that

optimization of fluidic oscillators becomes an easier option with computer-based studies, as any desired modification in their geometry can be easily introduced.

Considering that their simplicity guarantees reliability and money-savings and that it improves the current competitors' characteristics, it will probably stand out as soon as applications in real life are feasible. This is why this study attempts to gather as much reliable data as possible regarding further investigation in the field, even for future experimental research. Remarks must be made upon the fact that there is already a line of investigation in progress on fluidic oscillators in Escola Tècnica Superior d'Enginyeries Industrial i Aeronàutica de Terrassa (ETSEIAT), as mentioned before. This work is part of this investigation, being a continuation of the works performed by Ruiz [8] and Sarmiento [17], with the aim of enlarging the available data with a new device.

Chapter 2

State of the art

In 1800, Young noticed the wall attachment phenomenon [18] although it was not until the 1930's that Henri Coanda patented a device that made use of the so-called "Coanda effect", which describes the fact that a jet of fluid tends to attach to a nearby wall when close enough [19]. This effect is one of the fundamentals on which fluidic oscillators are based.

It was in the 1960's that the first fluidic oscillators were developed, evolving out of research in fluid amplifiers for fluid logic purposes. They were initially conceived as logic gates with moderate gain, referred to as bistable Flip-Flop devices [20]. Several logic components and their working principles are detailed by Kirshner and Katz [21]. However, their use in logic circuits finally decayed in favour of the current electric devices.

Despite the loss of interest in fluidic oscillators for fluid logic, their possibilities for flow control enhanced their development, considering their significant advantages in front of competitors (which are more deeply discussed later) such as absence of mechanical components, wide range of materials availability, low costs and reliability [22]. In 1970, Viets [23] developed oscillating jet nozzles that could oscillate at frequencies of <500 Hz. However, the current technology shows a clear tendency to design smaller devices that can perform at higher frequencies, in accordance with the fact that in aerospace applications the minimal interference is always sought. For example, in 2004 Raman and Raghu [24] designed a miniature device capable of attaining frequencies of 3 kHz. Simões et al. [25] presented in 2013 a microfluidic oscillator with critical dimensions of 280 μm and maximum frequencies of 16,7 kHz, and Sullivan et al. [15] claim that some devices produce a 325 μm wide oscillating jet at frequencies over 22 KHz with mass flow rates of the order of 1 g/min. In any case, those smaller devices have the handicap of giving lower momentum transfer due to the lower mass flow rates, although it is not

a critical drawback. Figure 2.1 illustrates the typical dimensions of a miniature fluidic oscillator.

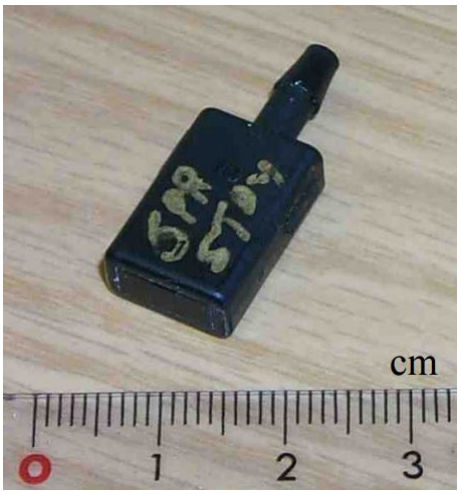

FIGURE 2.1: Fluidic oscillator dimensions [2]

As far as applications are concerned, one major application was found in flow measurement: their ability to oscillate in specific frequencies depending on the mass flow input widened their use and still allows this technology to be in use currently [25, 26]. Another important application has been found in windshield washer fluid dispensers in cars [27]. The oscillation of the exiting fluid enables a good range of dispersion of the washing fluid in car windshields. Finally, among many other applications: cavity resonance suppression [24], medical applications [28], use of fluidic oscillators as dynamic calibration tools [29], thrust vectoring [1], enhancement of jet mixing [16] (figure 2.2) and boundary layer control [5].

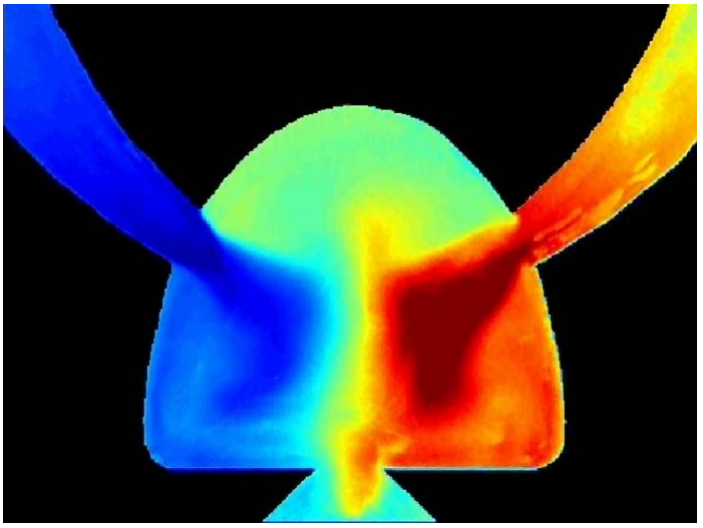

FIGURE 2.2: Fluidic oscillator aimed at jet mixing enhancement [3]

New fluidic oscillators that do not make use of the wall attachment effect have also been designed (figures 2.2 and 2.3 are two examples). Those oscillators are based on

fluid-dynamic interactions between two different jets introduced in a mixing chamber. Raghu et al. [3] provide bibliography and a study of a device of that kind.

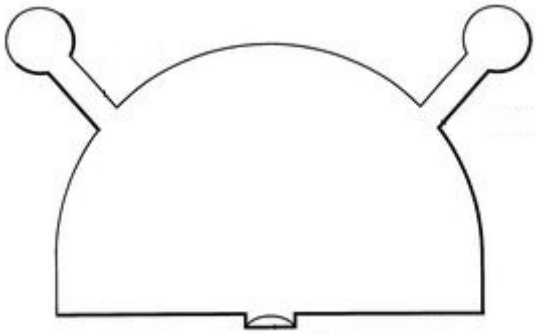

FIGURE 2.3: Fluidic oscillator without feedback loops [4]

Finally, the study of fluidic oscillators has been evolving with new technologies. Fluidic oscillators have historically been studied by experimental means, being usually their final performance the centre of interest. Nevertheless, many authors have focused in the characterization of the flow through the fluidic oscillator: Gregory et al. [30] used pressure transducers, water visualisation and Pressure Sensitive Paint. Sakaue et al. [2] also used PSP and discussed its reliability. Nevertheless, there are recent studies using numerical analysis like Simões et al. [31], with the aim of analysing the flow characteristics inside a fluidic oscillator without experimental expenses.

Chapter 3

Fluidic oscillators

In this chapter the background required for the understanding of the fluidic oscillators and their applications is provided. In the first section, the basic principle of the fluidic oscillators is explained: the wall attachment effect. Then, the geometry, the functioning and the different type of oscillators are described. Finally, the applications of the fluidic oscillators in the aeronautical field are presented, considering boundary layer control for stall and drag enhancing, as well as the current competitors.

3.1 Wall attachment effect

The so-called Coanda effect states that a jet of fluid flowing near a wall will attach to it as long as the wall is not excessively short, has a steep angle or is too far away. It was first discovered by Young in 1800 and Henri Coanda patented a device which made use of this phenomenon in the 1930's.

The basic idea is that a jet emerging from a nozzle near a wall entrains the initially stationary fluid that is confined between the jet and the adjacent surfaces which prevent the entrance of fluid from outside. As a result, a low pressure region is created between the jet and the wall, so the jet is forced to bend to the wall due to the pressure differential between its two sides (for now, it is assumed that there is only one wall in one side of the jet and the other side is free for simplicity reasons). In fact, a counterflow develops from the downstream, entering into the low pressure region in order to compensate the exiting mass flow corresponding to the entrained fluid. However, there still is a slight pressure reduction (figure 3.1). As the jet bends towards the wall, the counterflow is partially blocked by the deflected jet so the pressure lowers down even more until a closed bubble of fluid is generated. The equilibrium is reached when the mass flow coming from the

jet due to the vortex generated inside the bubble is equal to the mass flow going out of the bubble owing to entrainment.

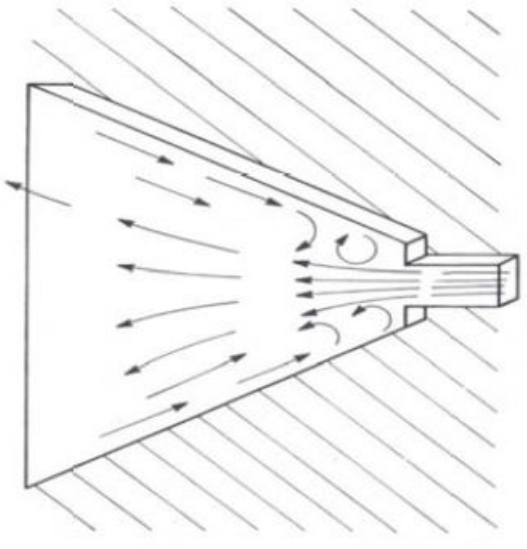

FIGURE 3.1: Wall attachment process with fluid entrainment and counterflow (Gi-Hun Kim [5]).

In a fluidic oscillator, originally the jet flows on the symmetry line, although at some point a little perturbation due to turbulence destroys the symmetry of the problem and the jet bends to one of the two walls through the process explained above.

3.2 Description

First of all, it is important to describe the main parts of the oscillator, and after that, the working principles are explained.

3.2.1 Geometry

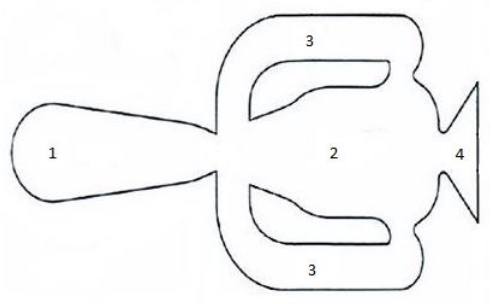

FIGURE 3.2: Geometry of the fluidic oscillator studied in the present work. Adapted from Raghu et al. [1]

Figure 3.2 illustrates the original oscillator provided in the paper by Raghu et al. [1]. The numbering shown in the image refers to each part of the geometry:

1. Inlet: Also called power nozzle or supply. Entry of the flow in the oscillator.
2. Interaction region: Also called mixing chamber. It is the zone where the flow enters after the inlet. The Coanda effect occurs there, with the jet attaching to one of its walls or the other alternatively.
3. Feedback channels: Also called feedback paths, feedback loops or recirculators. Essential for the oscillation of the device. Part of the flow attached to one wall of the interaction region enters the feedback channel from its further end (the one which is further from the inlet) in the form of an overpressure flow, and discharges into the mixing chamber from its nearer end (the one which is closer to the inlet). As a result, the jet entering the interaction region is deflected towards the other wall and the wall attachment is finally moved to the other side of the chamber.
4. Outlet: Exit of the flow in the oscillator.

3.2.2 Working principles

Fluidic oscillators are devices with no moving parts carefully designed so that its geometry causes the exiting flow to oscillate with a certain frequency. Figures 3.3 and 3.4 show examples of fluidic oscillators.

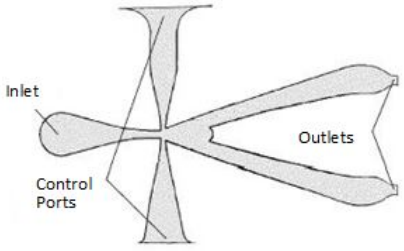

FIGURE 3.3: Fluidic oscillator (Yang [6])

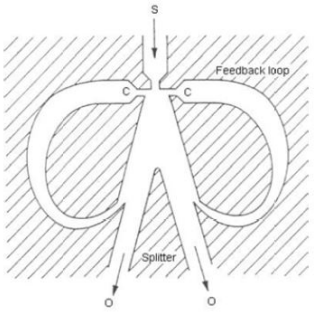

FIGURE 3.4: Fluidic oscillator (Morris [7])

The reason for the oscillation is actually simple. The incoming flow enters the interaction region and because of the "Coanda" effect the flow attaches to one side of the chamber. Then, the exiting jet is also deflected on its way out, thus having an exiting flow that is not parallel to the symmetry line. However, part of the flow that is attached to one wall is suctioned through the feedback channel in its donwstream entry (see figure 3.5).

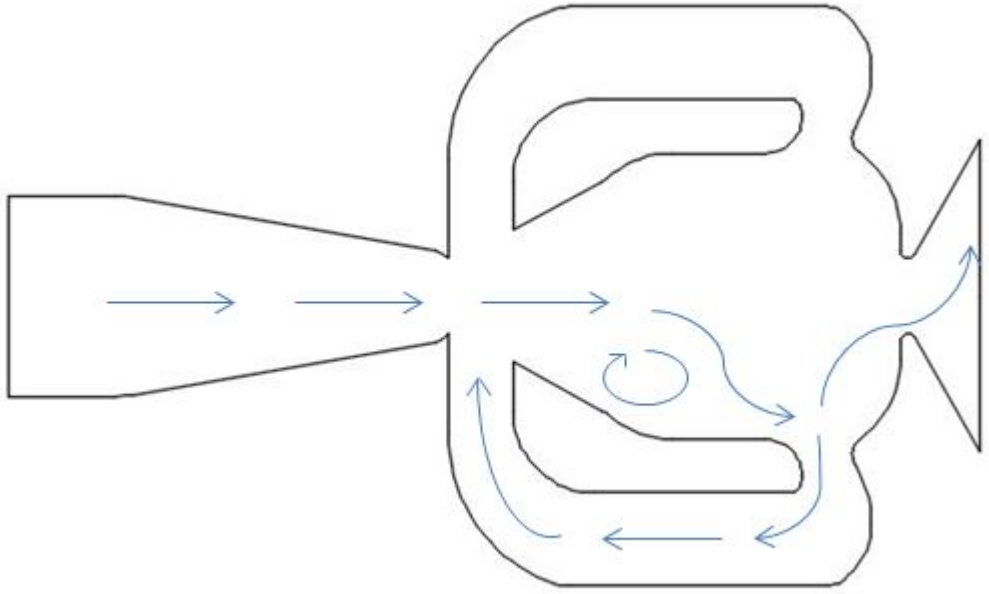

FIGURE 3.5: Flow at phase 0º

This overpressure finally exits the feedback channel in the upper entry, colliding perpendicularly with the incoming flow in the interaction region and then turning its attachment to the opposite-side wall. Obviously, the exiting flow will now be deflected to the other side as well. Then, part of the flow attached to the new wall is suctioned by the feedback channel, exiting in its upper entry and deflecting the flow again to complete one cycle of oscillation (see figure 3.6). This is repeated in a certain frequency depending on a lot of variables such as the angle of the outlet nozzle or the amplitude of the inlet nozzle [17].

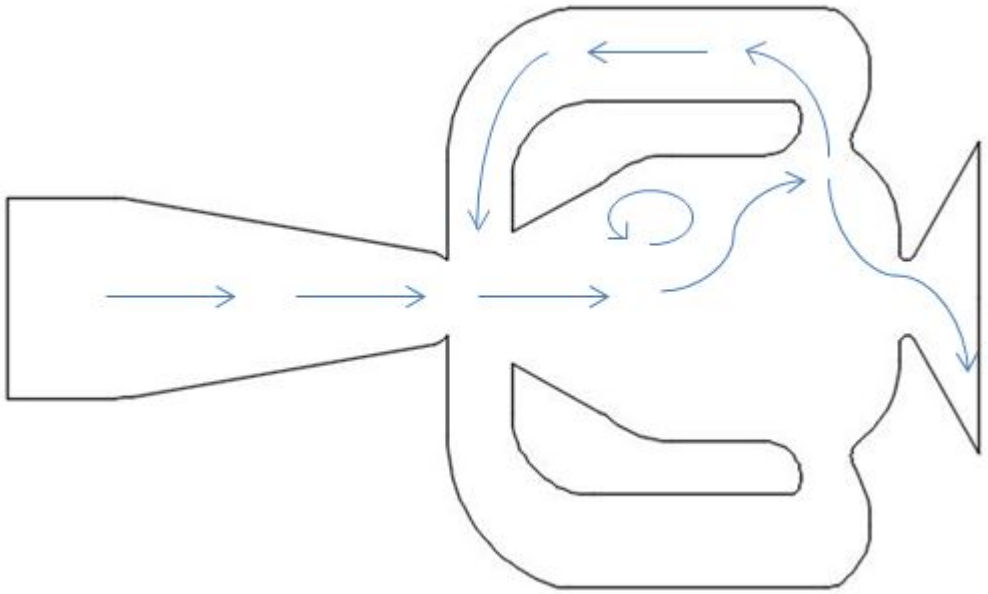

FIGURE 3.6: Flow at phase 180º

3.2.3 Types

There are basically 2 types of fluidic oscillators: based on wall attachment effect and based on jet interaction. The explanation above is referred to the first type of oscillators, as the fluidic oscillator studied here belongs to that group. However, the oscillators belonging to the second group rely solely on the fluid dynamics of the interaction between two jets of flow, and do not have feedback channels. For example, the oscillator in figure 3.3 belongs to that group. Notice that it is quite similar to the first group of oscillators, as the control ports resemble feedback channels. Nevertheless, they do not work in the same way. The use of feedback channels provides a given oscillation, while injection or suction of fluid through the control ports in an asymmetrical way (one of them injects fluid while the other one is suctioning and vice-versa) is responsible for the oscillation in this case. Obviously, it requires external power to supply pressure differentials in the control ports.

Some other fluidic oscillators belonging to the second group do not have anything similar to the feedback channels or control ports. They consist in a mixing chamber with two inlets where the pure fluid interaction and the rate at which the jets enter the chamber provides the final oscillation. Figure 2.3 illustrates a device of that kind.

3.3 Aeronautical applications

This study is focused on aeronautical applications, so the fundamentals of aerodynamics in which the fluidic oscillator is involved are explained in this section. In addition, the current competitors in the field are also enumerated here.

3.3.1 Boundary layer

The usual approach of the study of a moving object in a fluid consists in representing the object as static whereas it is the fluid that is actually moving. Thus, the fluid is assumed to be moving at a certain speed v while the object is at speed 0. Then, an essential boundary condition is that the surface of the object is at 0 speed, so due to viscosity the extremely thin layer of fluid contiguous to the wall that wets it must be also at 0 speed, while the adjacent layers of fluid are progressively at higher speed until the last one reaches v.

This aggregate of layers is called boundary layer, and is usually very thin compared to the object dimensions, while the rest of the fluid is considered the "far" flow field. Due to viscosity, the change in speed must be progressive, the contiguous layers of fluid

cannot have big velocity gradients, so this is why the boundary layer exists, and it has a crucial role in aerodynamics. The thickness of the boundary layer is normally defined as the distance from the surface at which the speed reaches 99% of the speed in the far field (freestream conditions). Figure 3.7 and figure 3.8 illustrate this effect.

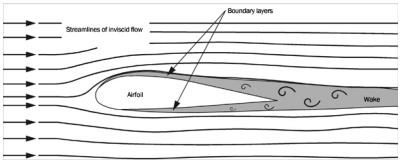

FIGURE 3.7: Boundary layer illustration in grey colour(Pérez-Herreras [9])

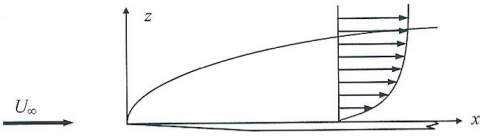

FIGURE 3.8: Detail of a laminar boundary layer. Velocity gradient. (Meseguer and Sanz [10])

There are 2 types of boundary layers: laminar and turbulent. The laminar boundary layer is found at low speed. It consists of a very neat and smooth flow, with well defined streamlines. It creates less skin friction and consequently less drag. However, it is more unstable because of its low energy: it is more easily broken down and then more drag is generated if such point is reached. On the other hand, the turbulent boundary layer is more commonly found at very high speeds, around wrinkled surfaces or after the transition of the laminar layer into a turbulent layer at a certain distance of the leading edge of a surface. It consists of a chaotic flow with swirls, very energetic and with a lot of momentum transfer. Given that, it creates more frictional drag, although its higher energy due to its chaotic behaviour guarantees more stability and allows the flow to stay attached to a surface longer than the laminar boundary layer. This is why the transition of the boundary layer from laminar to turbulent is always sought in aeroplanes, but also sought to be as far aft on the wing as possible. Figure 3.9 shows an experiment where the two different behaviours are easily visualized with a filament of ink inside the flow.

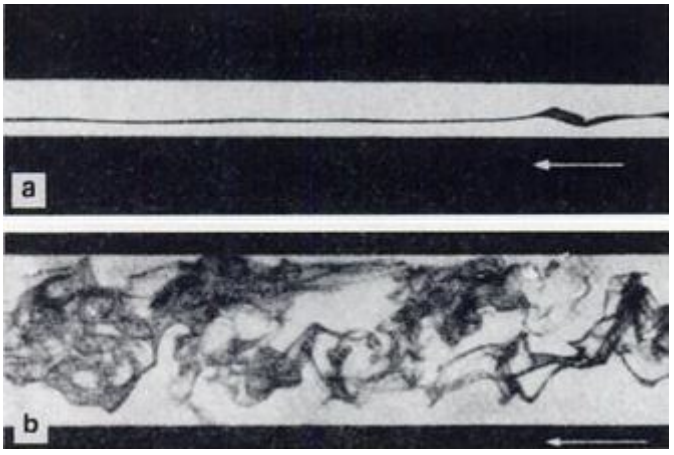

FIGURE 3.9: Flow in water made visible by a coloured filament, by W. Dubs in 1939 (Schlichting and Gersten [11]). a) Laminar flow, Re=1150 and b) Turbulent flow, Re=2520

The reasons for the characteristics of the 2 types of boundary layers are based on the different velocity profiles that each one of them has. The turbulent boundary layer has a fuller profile due to its higher mixing inside, having a big velocity gradient near the wall (figure 3.10.b), while the laminar layer has a more constant gradient (figure 3.10.a).

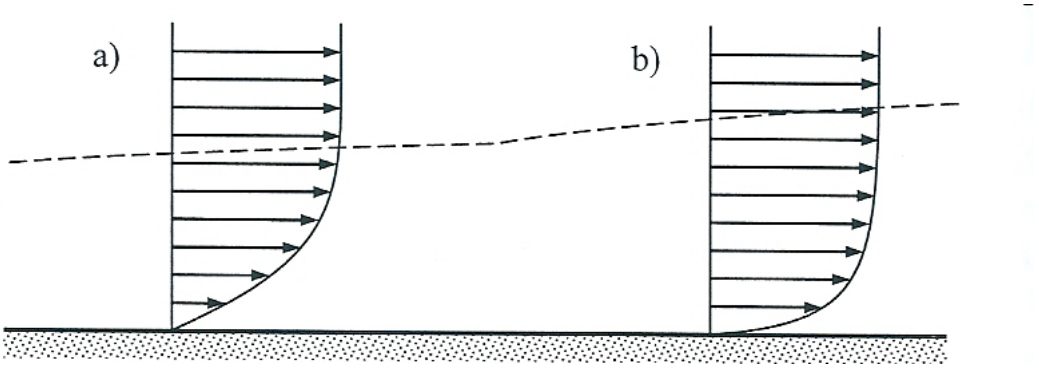

FIGURE 3.10: Typical velocity profiles in a a) laminar boundary layer and b) turbulent boundary layer. Meseguer and Sanz [10]

Apart from that, it is important to remember that the friction drag depends on the shear stress on the wall, defined as follows:

$$\tau_w(x) = \mu(\frac{\partial u}{\partial y})$$

Where the x axis is parallel to the wall and y axis perpendicular, so that the friction drag finally depends on the velocity gradient perpendicular to the wall. In regards of what has just been said about each kind of profile, it is clear that the turbulent boundary layer, which has stronger gradients, will have higher friction drag than the laminar layer, while this same characteristic provides higher resistance to the adverse pressure gradients and thus more stability in front of boundary layer separation.

The limit between each type of boundary layer is established through the use of the Reynolds number:

$$Re = \frac{\rho v L}{\mu} = \frac{vL}{\nu}$$

Where ρ stands for the density, v the freestream velocity, L a characteristic length of the problem, μ the dynamic viscosity, and ν the cinematic viscosity of the fluid.

This number establishes the quotient between the convective terms and the viscous terms of the Navier-Stokes equations that define the movement of the fluids, being a relation between the inertial and the viscous forces on the flow. A critical Reynolds number can be found for each different situation, corresponding low Reynolds numbers to laminar flow and high Reynolds numbers to turbulent flow. For example, in circular ducts the typical critical number is between 2000 and 3000. Notice that the Reynolds number

depends on a characteristic length of the body, so a boundary layer that has to cover a long surface is likely to start being laminar but finally transitioning to a turbulent flow.

In presence of an adverse pressure gradient the layers that are closer to the wall decelerate more than the far ones: the near layers have less momentum, owing to the fact that momentum is continuously transferred to the wall in the form of friction, so they have more difficulties in overcoming the adverse pressure gradient. After keeping advancing, the near layers are decelerated more and more until they reach 0 speed or even return backwards (figure 3.11). This effect becomes more important with time, affecting more layers until the whole boundary layer is separated from the wall. In a wing this creates stall, and it is disastrous as it destroys the lift that the wing is supposed to generate and the aeroplane falls, apart from dramatically increasing drag.

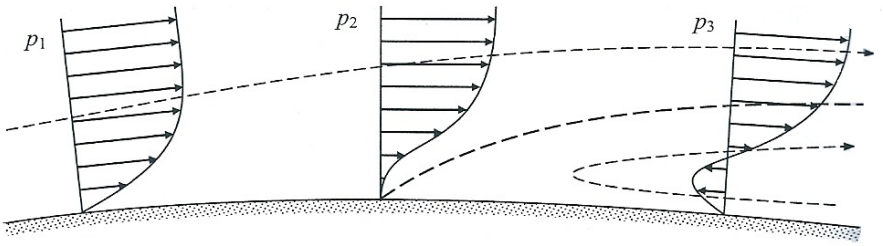

FIGURE 3.11: Typical velocity profiles in front of an adverse pressure gradient ($p_1 < p_2 < p_3$). Boundary layer separation. Meseguer and Sanz [10]

The importance of the fluidic oscillator in this field is in boundary layer control, in order to reduce drag and allow performance of wings at higher attack angles without stall, thus increasing the lift coefficient continuously, without the current limit (further explanations of both effects are found in the following sections). This can be achieved by the introduction of a more energetic and oscillating jet in the flow that enhances mixing and retards separation. The fact that the jet is oscillating greatly enhances the separation retarding effect (see Schlichting, H. and Gersten, K. [11]), emulating a device capable of blowing and suctioning alternatively. Moreover, the control of the boundary layer transition can provide the most efficient combination of laminar and turbulent layers for friction drag minimization.

3.3.2 Stall

The stall of an aeroplane establishes a critical performance point that cannot be surpassed, limiting the lift that a wing can generate. As seen before, if strong adverse pressure gradients are found, the boundary layer can separate from a wing and then it enters a stall where it is no longer able to generate lift to keep flying while the drag becomes extremely high. Of course, the main importance of the stall comes from the

fact that if the wing does not generate lift the aeroplane falls and could have an accident if the pilot cannot recover from the stall. However, pilots always try to avoid stall and have many warnings with that purpose, so in general it is not a problem.

On the other hand, another point of view can be used: if the stall could be retarded, the maximum lift attainable by a wing could be also increased, thus enabling the aeroplane to perform all manoeuvres at lower speed and save fuel. In addition, it could provide the plane with higher response capability in case of an emergency, having higher climb rates and so on. Moreover, if take-off and landing were performed at lower speeds, runways could be shortened and the possibility of an accident, or at least a fatal one, could be reduced.

When a 2D profile is at a certain angle of attack α it generates lift due to the pressure differential between the top and the low part of the profile, where the lower surface pressure is higher than the upper surface pressure (for simplicity purposes the profile is supposed to be at a positive angle). However, as α is increased, an adverse pressure gradient is grown near the leading edge, until it is so high that it can cause the separation of the boundary layer as explained in the previous section. Besides, considering that the pressure gradient depends generally on the thickness of the profile and the fact that the negative pressure gradient is located near the leading edge, one of the following situations can be found:

- Definitive separation of the still laminar boundary layer
- Separation of the still laminar boundary layer with subsequent reattachment
- Transition from laminar to turbulent boundary layer followed by separation of the turbulent layer
- Transition from laminar to turbulent boundary layer with no separation

In a thin profile the pressure gradient near the leading edge is higher than in a thick one, so they are more likely to encounter separation while being the boundary layer still laminar, either with reattachment or not. On the other hand, in a thick profile the boundary layer will probably transition to turbulent first and then separate or not depending on the shape of the profile and α.

As for reattachment, the laminar flow early separated turns into the more chaotic and energetic turbulent flow, thus enabling it to reattach forming a recirculation bubble (remember that the turbulent flow easily transmits momentum between the different layers, so it is easier for the turbulent flow to reattach). Figure 3.12 illustrates this

phenomenon. Apart from that, the Reynolds number also influences reattachment: a higher Reynolds shortens or removes the recirculation bubble by advancing the transition point to turbulent flow, while a lower Reynolds can enlarge it until there is no longer reattachment and the flow is definitively separated.

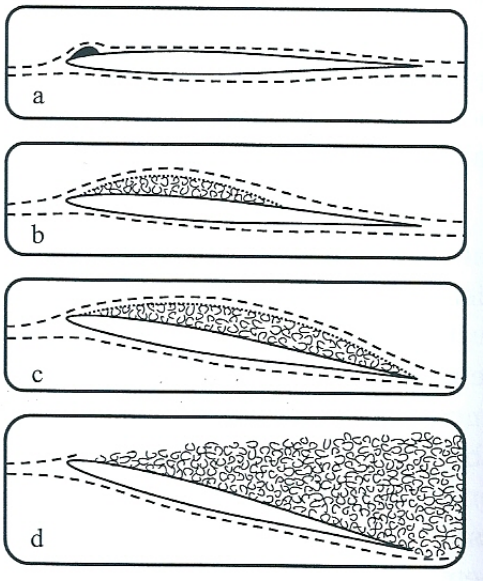

FIGURE 3.12: Boundary layer separation with reattachment depending on α. a) Formation of a small bubble with early reattachment, b) Further boundary layer reattachment, c) Boundary layer reattachment at the trailing edge and d) Boundary layer separation. Meseguer and Sanz [10]

The problem with the separated region is that the pressure in that region lowers down (which is in fact beneficial for lift) but a side-effect is that the suction peak in the leading edge is reduced. When α continues to increase the adverse pressure gradient is increased and the separated region is extended so it finally reaches a critical point when either all the upper surface is separated or the total pressure balance does not provide enough suction to maintain the aeroplane in the air. Moreover, the low pressure in the rear part of the wing increases the drag, as there is higher suction backwards in the X direction as well.

3.3.3 Drag

Drag is classified in different groups according to its origin and the type of physical principle involved (table 3.1):

Origin	Viscous		Potential	
Type	Friction	Pressure	Induced	Wave

TABLE 3.1: Drag classification

Aerodynamics is usually studied in two different ways: potential analysis and viscous analysis. The potential analysis is the first approach and it does not consider the viscosity of the fluids, while the viscous analysis is performed afterwards and incorporates the effects of viscosity in the system (as seen before, viscosity is the reason for the existence of the boundary layer). The potential analysis consists of a mathematical formulation of the Navier-Stokes equations neglecting all the terms related to viscosity, thus simplifying them enormously. This provides a simple solution, called potential solution, that defines very well the flow in the "far-field" region. However, it does not explain the existence of drag in some problems (the well-known d'Alembert's paradox proves that the drag force on a moving object in an incompressible and inviscid flow is 0). Then, it is the viscosity with the addition of the boundary layer to the problem that provides a better solution considering drag, by friction forces and by pressure or form forces. This is why these are included in the viscous classification, and they are the important ones in the present study.

Friction drag

Friction drag, as briefly mentioned before, is caused by the boundary layer, where momentum is exchanged between the "far-field" and the surface of an object. This momentum transferred to the object is finally translated into a shear force in its surface, the so-called friction drag. It is also important to highlight that the turbulent layer has a higher friction drag than the laminar one, owing to the fact that there is higher momentum exchange in the turbulent boundary layer.

Pressure drag

Pressure drag, also called form drag, is caused by boundary layer separation. The separated region of the boundary layer can be quite big, especially in blunt bodies where huge adverse pressure gradients can occur, and as seen before, the separated region has low pressure. Hence, the pressure difference between the upstream and the downstream part of the object creates drag. This is why it is called pressure drag, while the name form drag is due to the fact that it greatly depends on the object shape. Pressure drag is the most important source of drag in most applications, especially on ground. Figure 3.13 illustrates the difference in pressure drag between a streamlined and a blunt body.

As for potential drag, it is not really important in the present study. Induced drag is a 3D effect caused by interference between the upper and the lower side of a wing and turbulent wake deflection, involving a misalignment of the aerodynamic force that generates a new drag component. On the other hand, wave drag is an effect found in compressible flow due to the presence of shock waves.

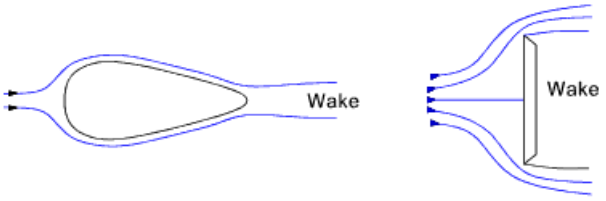

FIGURE 3.13: Comparison of flow separation and drag on streamlined and blunt shapes respectively. From roymech.co.uk

3.3.4 Competitors

It is important to briefly review the current most commonly used technology that can compete with the fluidic oscillator and see if the introduction of fluidic oscillators in the market is feasible. Those competitors are all boundary layer actuators, like the fluidic oscillators, and are focused on drag reduction and lift enhancement (high lift devices).

Apart from that, the devices can be also classified into active or passive. Active devices are those which require power for their functioning. Passive devices are those which always work without any external action. Of course, the main advantage of the passive devices is that they do not consume energy.

- Slot: passive device where a duct communicates the lower and the upper sides of a profile so that some air is blown from the lower part of the profile to the upper zone, adding momentum to the boundary layer in order to retard separation or reduce pressure gradients. Used for high lift and drag reduction purposes.
- Flap: passive device located at the trailing edge of the profile. There are many different types of flaps but the general idea is that they increase the curvature and the surface of the profile as well as slight modifications of the angle of attack. These effects generate an increase in the lift coefficient of the profile. In addition, some of them have slots in order to retard separation. Their use is worldwide extended and all or almost all aircraft carries flaps. Used for high lift purposes. There even exist blown flaps that use the jet from the engine to act on the boundary layer.
- Slat: passive device located at the leading edge of the profile. Same principles as the flap and some have slots as well, although the blowing is done at the leading edge, thus softening the adverse pressure gradient. Very extended use in big aeroplanes as well. Used for high lift purposes.
- Boundary layer blowing: active technology based on the same principles as the slot but in a different manner. There is a pressure supply inside the wing that can blow air to the upper side of the profile instead of a communication duct.

- Boundary layer suction: active technology similar to the blowing devices, although suction is used instead. The low energy region of the boundary layer is suctioned by an artificially generated low pressure chamber inside the wing so that boundary layer separation is retarded.
- Vortex generators: passive device placed on the wing, consisting of a small vane vertically attached with a certain angle with respect to the air with the aim of generating vortex and enhancing the transition to turbulence.

On the other hand, fluidic oscillators present significant advantages in front of those devices that make them a very interesting alternative in order to have more efficient vehicles:

- Small size. Some of them are of the order of μm, so they have a good integration and low interference.
- Lightweight
- Absence of mechanisms or moving parts
- Although some of them are active and some passive devices, the energy requirements even in the worst cases are negligible in front of other devices.

Thrust vectoring is another application under development of the fluidic oscillators that does not involve boundary layer control. Current technology uses either panels to deflect the exiting jets of the engines or even the rotation of exit nozzles. Those mechanisms are usually very complex, inefficient, big and heavy (since they must withstand high forces). Otherwise, the vectoring nozzles require complex mechanisms and moving parts and are usually expensive. Fluidic oscillators have all the advantages detailed above while it has been proved that they can deflect jets substantially [1], so they also provide another important alternative to the current technology.

Regarding that, it is clear that fluidic oscillators provide a good solution for boundary layer control, enhancing performance of the aeroplanes by increasing lift, reducing drag and delaying stall. In addition, other applications out of the aeronautical fields are very interesting, such as combustion mixing enhancement, which can save big amounts of fuel. Moreover, the reduction in weight when replacing other devices might lead to more fuel saving. Finally, applications in drag reduction in ground transportation vehicles such as cars, trucks or trains is an exciting possibility that justifies further investigation.

Chapter 4

Specific studies significant to the present work

In this chapter, the 2 studies mentioned in the introduction are analysed. There is one study (Ruiz [8]) that belongs to the line of investigation in progress in ETSEIAT and, in fact, constitutes the foundations of the future investigations in this field.

The second study (Raghu et al. [1]) is the reference paper from which this work starts. In this paper, the fluidic oscillator studied here was experimentally analysed. Therefore, the conditions of the experiment and the results have to match with the numerical analysis performed now, but before, a summary of the most important aspects of each work are highlighted in the following sections.

4.1 Line of investigation in ETSEIAT

In 2014 Mikel Ruiz Arozarena performed a study of a fluidic oscillator in "Estudio de osciladores fluídicos mediante mecánica de fluidos computacional" [8]. It was the first study in ETSEIAT dealing with fluidic oscillators. It had 2 fundamental goals: on the one hand, a fluidic oscillator studied experimentally in Technische Universität Berlin by Bobusch et al. [12] was analysed with a numerical approach; on the other hand, it intended to identify the most significant parameters that allow a correct numerical simulation. Having said that, only the results corresponding to the second objective are reviewed here, as the first objective is not relevant to the present work.

Bobusch , Woszidlo, Bergada, Nayeri and Paschereit in 2013 [12] studied the behaviour of a fluidic oscillator (shown in figure 4.1) under various conditions: water was used as the working fluid and a range of Reynolds between 8711 and 16034 was studied. In

addition, a numerical study was also carried out in order to compare the results and find the best model for the simulation. The final suggestion of this study was to use the SST model (Shear Stress Transport) and Ruiz [8] confirmed this conclusion.

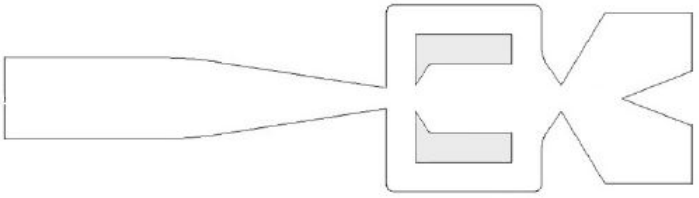

FIGURE 4.1: Fluidic oscillator studied by Bobusch et al. (2013) [12] and Ruiz(2014) [8]

Ruiz meshed the geometry studied by Bobusch et al. [12] and ran a mesh independence test, which tried to check if further refinements of his meshes led to higher precision of the results. Thus, a mesh that allows precise results within short computing times can be obtained. Three different meshes were used: one with 70000 nodes, one with 120000 and the finest one that had 210000 nodes. Ruiz verified that the coarse mesh could not achieve precise enough results, although the computing time was very low. However, both the other two meshes provided similar results with a substantial difference in computing time, so Ruiz finally concluded that the best mesh was the one that had 120000 nodes. In fact, the convergence test showed that it would even be better to test finer meshes, although the time constraints forced him to use the 120000 nodes mesh. In the present work, this results are regarded as a reference, so meshes around 200000 nodes are expected. Table 4.1 shows the results of the mesh independence test by Ruiz [8]:

	Coarse mesh	Medium mesh	Fine mesh
Number of nodes	70000	120000	210000
Computing time	10h	1day 10h	3days 2h

TABLE 4.1: Results of the independence test carried out by Ruiz [8]

After verifying that the mesh was fine enough and after computing the simulation time needed for each mesh, different solution methods were tried: SST, k-epsilon, k-omega and RSM. Ruiz [8] agreed with the conclusion made by Bobusch et al. [12], which was that the best model for the simulation is the SST, regarding its accuracy in results and its low computational cost in comparison with the other options.

Ruiz reproduced the experiment with only slight differences. He concluded that those differences might be owing to the lack of the third dimension in his analysis, but also that the numerical analysis can be used as a reliable approach to study fluidic oscillators.

4.2 Experimental analysis by Raghu et al.

In 2005 G. Raman, S. Packiarajan, G. Papadopoulos, C. Weissman and S. Raghu studied the use of fluidic oscillators for thrust vectoring in "Jet thrust vectoring using a miniature fluidic oscillator" [1]. The aim of the paper was obviously to redirect a jet by placing fluidic oscillators next to the exit nozzle.

Several techniques were used in order to collect data. The oscillatory near-field hydrodynamic pressures were measured using a Bruel and Kjaer 0.635cm microphone. Detailed flow field data was acquired using PIV technology and a pitot probe. The volume flow was measured with mini-rotameters and the mass flux was estimated with the calculated densities. Moreover, the flow was seeded with water 1-2 μm droplets in order to better visualize it.

Before performing the thrust vectoring experiment, the fluidic oscillator was separately tested in order to know its capabilities. According to the paper, "The fluidic actuators used had no moving parts and produced oscillatory flow with a square wave form at frequencies up to 1,6 kHz". The range of pressures studied was from 10 kPa to 165.47 kPa, with air as the working fluid. Figure 1.1 shows an image of the device used in this experiment, while figure 4.2 shows the resulting frequencies of the outlet flow depending on the inlet gauge pressure.

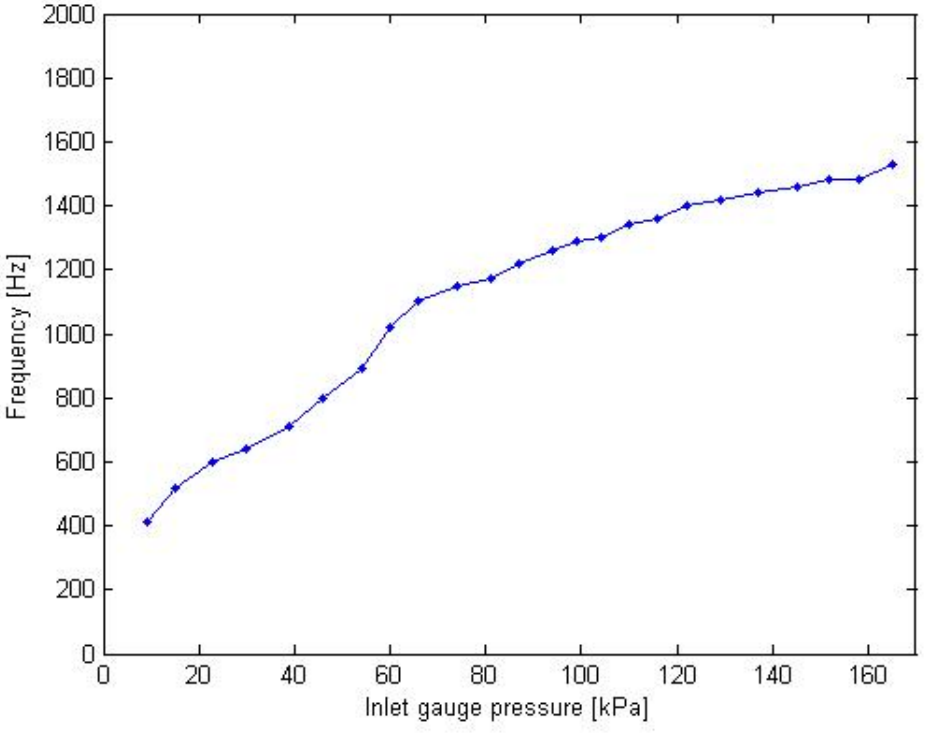

FIGURE 4.2: Outlet flow frequency vs inlet gauge pressure [1]

Another important parameter is the mass flow rate through the oscillator. Although there is no diagram nor much specific data about it, table 4.2 shows the few values of mass flow rates provided in the paper. Note that the data referring to an inlet gauge pressure of 206.80 kPa is out of the range of pressures mentioned before. The test of the fluidic oscillator alone was performed for a range of 10-165.47 kPa, while in the thrust vectoring experiment higher inlet pressures where reached. This value was obtained during the thrust vectoring experiment and it can be included in the present work as well.

Pressure (kPa)	Mass flux (kg/s)
10.00	$1.18 \cdot 10^{-4}$
20.68	$2.00 \cdot 10^{-4}$
62.04	$5.39 \cdot 10^{-4}$
206.80	$5.41 \cdot 10^{-3}$

TABLE 4.2: Mass flux of the fluidic oscillator vs inlet gauge pressure [1]

Figure 4.3 shows a regression of the mass flux in front of pressure in case the interpolation of unknown mass fluxes was needed.

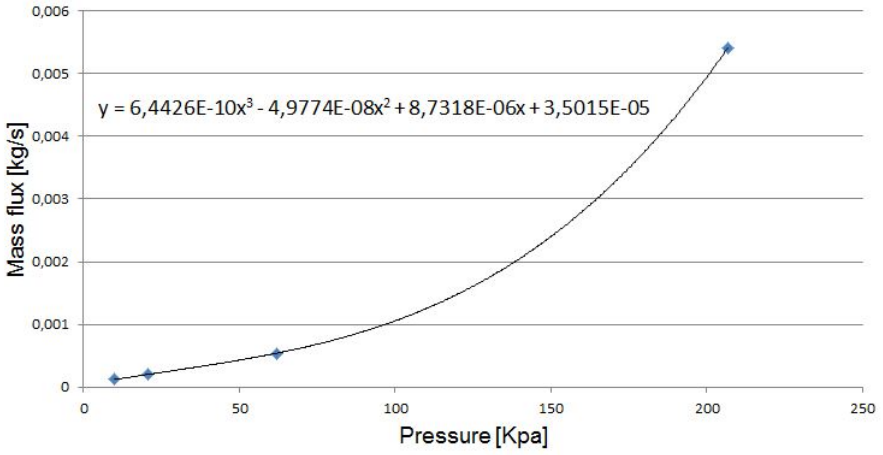

FIGURE 4.3: Mass flux vs inlet gauge pressure and polinomial regression

Chapter 5

Solver theory

In this chapter, the underlying theory of the solver used is explained. The procedure followed by the solver to compute the simulation is analysed and the most significant parameters of the solver are introduced in the first section. In the second section, the turbulence modelling chosen (Shear Stress Transport turbulence model) is explained.

5.1 General theory

The numerical simulation has been performed with ANSYS Fluent software. Before explaining the details of the simulation performed in this work, it is important to define the theory behind the solver so that the numerical simulation carried out by the software is understood.

ANSYS Fluent calculates the flow properties by solving a set of equations on each mesh node. For all flows, ANSYS Fluent solves conservation equations for mass and momentum while additional transport equations are also solved when the flow is turbulent. There are many other useful features of ANSYS although they are not necessary for this work. The Fluent solver is based on the finite volume method that consists in:

1. Division of the domain into discrete control volumes using the imported mesh
2. Discretisation of the governing equations in each control volume, hence transforming them into algebraic equations where the properties of the fluid are the unknown variables (velocity, pressure...)
3. Linearisation of the equations and solution by iteration

The equation for conservation of mass, also known as continuity equation, for a single-phase problem is:

$$\frac{\partial \rho}{\partial t} + \nabla \cdot (\rho \vec{v}) = 0 \tag{5.1}$$

The momentum conservation equation in an inertial reference frame is:

$$\frac{\partial}{\partial t}(\rho \vec{v}) + \nabla \cdot (\rho \vec{v} \vec{v}) = -\nabla p + \nabla \cdot (\bar{\bar{\tau}}) + \rho \vec{g} + \vec{F} \tag{5.2}$$

where p is the static pressure, $\bar{\bar{\tau}}$ is the stress tensor, $\rho \vec{g}$ is the gravitational body force and $\vec{F}$ represents the external body forces. The stress tensor is defined as follows:

$$\bar{\bar{\tau}} = \mu[(\nabla \vec{v} + \nabla \vec{v}^T) - \frac{2}{3} \nabla \cdot \vec{v} I] \tag{5.3}$$

where μ is the dynamic viscosity and I the unit tensor.

The energy equation is not used in the present analysis as it involves unimportant parameters to the study that suffer low variations (such as the temperature) and thus the computing costs can be reduced.

In general, any scalar transport equation that is used is solved by a control-volume-based technique, integrating the equation in a control volume and discretising it. The general unsteady conservation equation for transport of a scalar quantity ϕ can be expressed in its integral form on a control volume as:

$$\int_V \frac{\partial \rho \phi}{\partial t} dV + \oint \rho \phi \vec{v} \cdot d\vec{A} = \oint \Gamma_\phi \nabla \phi \cdot d\vec{A} + \int_V S_\phi dV \tag{5.4}$$

where ρ stands for the density, $\vec{v}$ the velocity vector $(u\hat{i} + v\hat{j})$, $\vec{A}$ the surface area vector, Γ_ϕ the diffusion coefficient for ϕ, $\nabla \phi$ the gradient of ϕ (which is $(\partial \phi / \partial x)\hat{i} + (\partial \phi / \partial y)\hat{j}$) and S_ϕ the source of ϕ per unit volume.

The discretisation of equation 5.4 yields:

$$\frac{\partial \rho \phi}{\partial t} V + \sum_f^{N_{faces}} \rho_f \vec{v_f} \phi_f \cdot \vec{A_f} = \sum_f^{N_{faces}} \Gamma_\phi \nabla \phi_f \cdot \vec{A_f} + S_\phi V \tag{5.5}$$

where N_{faces} is the number of faces enclosing the cell, ϕ_f the value of ϕ convected through face f, $\rho_f \vec{v_f} \cdot \vec{A_f}$ the mass flux through the face, $\vec{A_f}$ the area of face f, $\nabla \phi_f$ the

gradient of ϕ at face f and V the cell volume. Note that if the scalar quantity ϕ is 1 the continuity equation is obtained, while if ϕ is $\vec{v}$ the momentum equation is obtained.

There are two different approaches for the numerical solver: pressure-based and density-based. Both methods use the momentum conservation equations to obtain the velocity field. The difference lies in the fact that the density-based solver uses the continuity equation (equation 5.1) to obtain the density field and the equation of state for the pressure, while in the pressure-based approach the pressure field is extracted by solving a pressure equation or a pressure correction equation obtained by manipulation of continuity and momentum equations. Originally, the pressure-based solver was conceived for low-speed incompressible flows, while the density-based approach was aimed at high-speed compressible flows. However, nowadays both solvers are capable of solving a wider range of situations.

In addition, there are 4 possible schemes of resolution: SIMPLE, SIMPLEC, PISO and Coupled. The simplest schemes are SIMPLE and SIMPLEC, although SIMPLEC has instability problems for complex geometries and meshes with high skewness, which is the current case. On the other hand, the SIMPLE scheme is simpler than the PISO scheme and the Coupled scheme (apart from this, the Coupled scheme is recommended for steady-state problems). Figure 5.1 illustrates the pressure-based algorithm when the SIMPLE scheme is used.

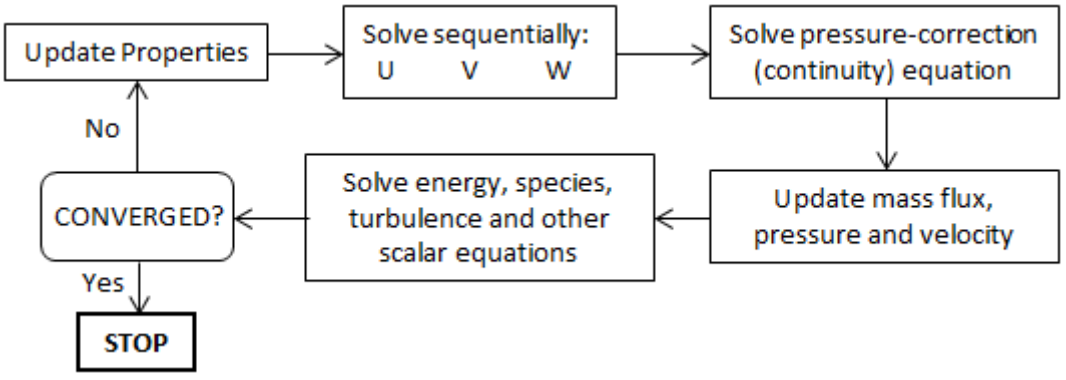

FIGURE 5.1: Pressure-based SIMPLE solver algorithm [13]

Considering the oscillatory character of the fluidic oscillators, a non-steady-state simulation is required. In a non-steady-state simulation variables change over time so the time-dependent terms of the equations must be accounted for. In addition, the solving procedure is slightly changed. The time is discretized into time steps, and the solution is sought for each time step. This means that the convergence algorithm in figure 5.1 is performed for each time step before advancing to the next time step. Nevertheless, a maximum number of iterations is usually set for each time step, so that the calculation

does not extend excessively over time. Thus, if convergence is not reached in the specified number of iterations, the time step is advanced to the next one. This implies that there must be more time steps than needed for the results, as the first time steps will not have reached convergence and must be discarded. Moreover, the time step elongation must be also established: it has been set at an order of magnitude between 10^{-7} s and 10^{-6} s so that it is approximately 3 orders of magnitude lower than the time needed for the completion of a cycle of the highest frequency expected. It is important to highlight that if too large time steps are used, convergence is usually more difficult to reach.

Apart from that, more solver parameters have to be fixed before running the simulation. It is not the aim of this section to deepen into the numerical solver theory and convergence principles, given their high complexity. However, based on personal experience, ANSYS Fluent user manuals [13, 32], suggestions made by the thesis director and the work performed by Ruiz [8], all the Fluent parameters have been set, leaving many of them at the default recommended option. The spatial discretisation, for example, has been set at First Order Upwind given that it is recommended for the flow being aligned with the mesh cells (which is true in most part of the current mesh) and it yields better convergence. However, the momentum discretisation has been set at Second Order Upwind and the pressure dicretisation at Second Order, in order to have higher precision in the results. This is achieved using a Taylor series expansion of the cell-centred solution instead of the average solution assumed for the First Order Upwind discretisation.

The convergence is determined by the residual values found in each equation solved by Fluent. When numerically solving a problem, after an iteration all values are put inside the equation in order to check the error. Equality is never reached in practice, there is always a difference between the left terms and the right terms of the equal sign of an equation. This difference is called the residual and it is the indicator of convergence. There is a moment when the difference is so low that the error is insignificant and convergence can be accepted. When the residual value is lower than the specified criteria, convergence is reached. In this study, the convergence criteria has been set at 10^{-5}, as suggested by Ruiz [8].

5.2 Turbulence modelling

As explained before, turbulence is caused by viscosity and it involves complex fluid flow, with large momentum exchange in its interior and with presence of eddies. Turbulence causes the formation of eddies due to the inertial forces dominating over the viscous forces. Initially, these eddies are large but they are constantly evolving into smaller eddies until the energy contained by the smallest eddy can be dissipated through molecular

diffusion. The dissipation of kinetic energy between the different length-scale eddies is represented by the dissipation coefficient ε. It is a time-dependent chaotic flow, which is the reason for the non-steady-state analysis. There is not an easy way to model it and there are not analytical solutions for the turbulent flow. The Navier-Stokes equations that describe the motion of a fluid do not provide exact solutions except for very simple specific situations. Even numerical solution of the Navier-Stokes equations for turbulent flow is infeasible due to excessive computing costs, so the usual approach is based on the time-averaged equations such as the RANS methodology (Reynolds-Averaged Navier-Stokes equations) together with turbulence models, such as the Spalart-Allmaras, $k-\omega$, $k-\varepsilon$ or SST. LES (Large Eddy Simulation) models are another alternative to RANS models but, although having better results, they are more expensive in terms of computational costs.

Thus, the RANS modelling of turbulence is based on statistical analysis: an average value is assumed, while another parameter accounts for fluctuations. A general scalar quantity in the Navier-Stokes equations is decomposed into $\phi = \bar{\phi} + \phi'$. Hence, the Navier-Stokes equations are rewritten with the new terms and then averaged, so that the final result is:

$$\frac{\partial}{\partial t}\left(\rho\bar{u_i}\right) + \frac{\partial}{\partial x_j}\left(\rho\bar{u_i}\bar{u_j}\right) = -\frac{\partial\bar{p}}{\partial x_i} + \frac{\partial}{\partial x_j}\left[\mu\left(\frac{\partial\bar{u_i}}{\partial x_j} + \frac{\partial\bar{u_j}}{\partial x_i} - \frac{2}{3}\delta_{ij}\frac{\partial\bar{u_l}}{\partial x_l}\right)\right] + \frac{\partial}{\partial x_j}\left(-\rho\overline{u_i'u_j'}\right) \tag{5.6}$$

Due to fluctuations, new terms appear that represent the effects of turbulence: the so-called Reynolds stresses $\left(-\rho\overline{u_i'u_j'}\right)$. The Reynolds stresses must be modelled in order to be able to solve equation 5.6. This is where the transport turbulence equations are needed.

As suggested by Ruiz [8] in his work, the $k-\omega$ Shear Stress Transport turbulence model is used. It is a combination of the $k-\varepsilon$ and the $k-\omega$ models, as it has a gradual change from the standard $k-\omega$ model in the inner region of the boundary layer to a high-Reynolds-number version of the $k-\varepsilon$ model in the outer part of the boundary layer. It benefits from the robustness of the $k-\omega$ model in the near-wall region and the free-stream independence of the $k-\varepsilon$ model in the far field. Moreover, the turbulent viscosity formulation is slightly modified with respect to the standard $k-\omega$ model in order to include the transport of the turbulent shear stress. The basic idea is that both models are mixed through an activation variable that is 1 near the wall (to fully activate the $k-\omega$ model) and 0 in the far field (to fully activate the $k-\varepsilon$ model).

Chapter 6

Computational analysis

In this chapter, the study performed in this work is detailed. All the aspects to consider and the simulations to be performed are explained here. On the first place, the geometry design is shown. On the second place, the mesh design process is detailed, commenting on the most critical aspects of this design and the final solutions used. In addition, a mesh independence test is done in order to identify which mesh can provide a balanced solution between accuracy and time requirements. Finally, the configuration of the simulations is explained in the last section.

6.1 Geometry

The geometry of the fluidic oscillator has been obtained from the paper "Jet thrust vectoring using a miniature fluidic oscillator" by Raghu et al. [1] (see figure 1.1). As seen in the image, only one measure is provided: the exit nozzle of the mixing chamber which is 0.14 cm. The depth of the fluidic oscillator is also specified (0.095 cm) but is irrelevant for the 2D study. Starting with this, the geometry has been measured as exactly as possible on paper and drawn with Autocad. Again, it is important to remark the fact that it is possible that the geometry provided by Raghu et al. [1] is slightly distorted with respect to the real one, so this could be a source of error for the results that needs to be considered.

ICEM-CFD program has been used for the geometry meshing. Importation of geometries to ICEM-CFD is not good, given that curves are not well reproduced and are very rugous, which is extremely harmful for the fluid dynamics occurring inside the geometry and could totally change the results. Then, the coordinates of some points have been extracted with Autocad and the geometry has been directly redrawn in ICEM-CFD with those coordinates, joining consecutive points with curves and straight lines.

It is important to define different parts of the geometry for the boundary conditions that must be set later in Fluent. In this study, the parts used have been: fluid region, inlet, outlet and wall.

6.2 Mesh design

Numerical analysis is useful for complex problems that are not solvable by analytical means, such as the Navier-Stokes equations that describe the motion of viscous fluids. As explained before, a numerical analysis is based on the discretization of the space into extremely small volumes (differential volumes) where the equations that define the problem are locally solved. Moreover, an iterative process is followed: an initial solution is first assumed for the domain of the problem; then, considering the initial properties assumed, each differential volume is solved and the new solution is incorporated; this process is repeated until the solution is converged.

A good mesh is essential for the solution of a numerical analysis. The mesh is the discretization of the space, given that it divides the domain of the problem into small cells. Obviously, a mesh with smaller cells, a fine mesh, is better than a mesh with bigger cells, a coarse mesh, due to the fact that it resembles more the ideal discretization into differential volumes and there is more precision in the solution. This is important because the bigger the cells are, the less resolution there is. That means that constant properties might be assumed for a big volume, a big cell, which in reality are not constant. However, there is a point of balance where there is enough resolution to correctly represent reality for the level of precision required in each case but the mesh is not excessively fine. A coarse mesh is more quickly solved, since the local solution of the equations must be repeated in less cells, so it is important to consider the computing costs of each mesh as well.

There are 3 types of mesh: structured, unstructured and hybrid. The structured mesh is very regular, all the cells have the same number of faces. In 2D, the cell in a structured mesh is quadrilateral. It is a highly efficient model in terms of memory space and usually has better convergence and higher resolution. An unstructured mesh is characterised by its irregularity. All shapes and connectivities are used in order to adapt to the most difficult geometries. It requires a lot of memory space but presents high adaptation to all situations. Finally, the hybrid mesh is a combination of the structured and the unstructured meshes, as regular regions make use of the structured mesh while some other complex regions use the unstructured mesh.

When designing a mesh it is important to distinguish the critical regions of the flow. A freestream flow is very simple and does not require a dense mesh in order to capture all of its characteristics. However, flow near a wall must be carefully meshed, as it involves boundary layer effects such as complex turbulence phenomenons. In fact, it is fundamental to accumulate a lot of cells, also called elements, near the walls and perpendicularly to the flow direction so that the characteristic velocity gradient of the boundary layer (mentioned in chapter 3) is correctly captured. Typically, the final design tends to have high density of elements near the walls, while the central regions, where the effects of turbulence are lower, can be adequately meshed with lower density of cells. Thus, the memory requirements are lower and so are the computing costs as well. Figure 6.1 illustrates this kind of design inside a duct with two limiting walls.

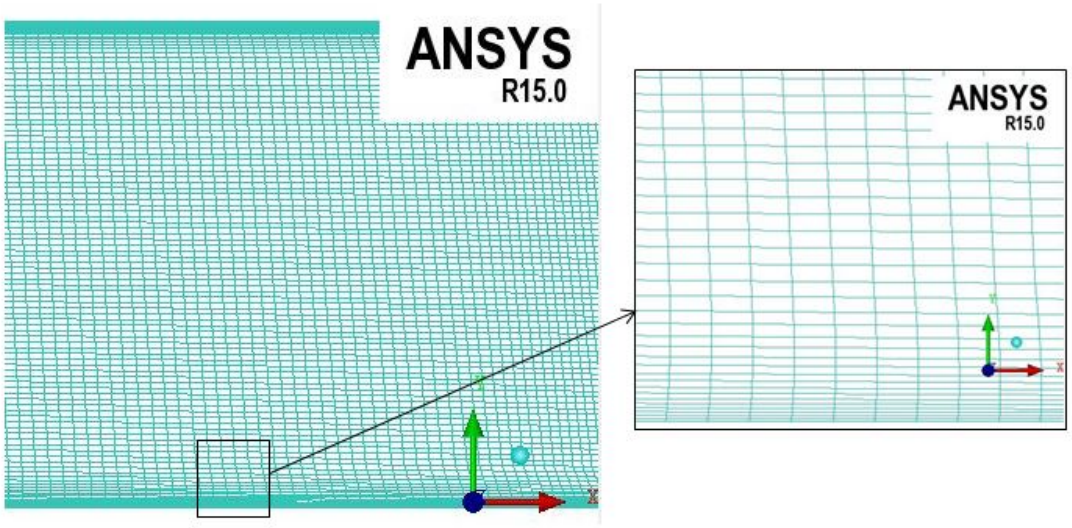

FIGURE 6.1: Boundary layer meshing

In addition to that, there are other requirements in regards of a good mesh design. It is important that contiguous cells do not have big size variations, so smooth transitions must be defined between regions of low density and regions of higher cell density. Aspect ratio is another significant parameter: the two dimensions of each cell must be as similar as possible, without having a side that is larger than the other one. However, if this cannot be achieved, it is better to have the larger side in the direction of the flow than perpendicularly. Finally, all the angles of the cell must be as close to 90^o as possible, with the minimum skewness. In conclusion, the idea is that the cells resemble squares as much as possible and that there are not big size jumps between consecutive cells.

As mentioned above, ICEM-CFD has been the program used for the mesh design. This program allows an approach based on blocking strategy, which is a variation of a structured mesh. The blocking strategy consists on dividing the geometry into rectangular regions called blocks and then associating these blocks to the edges of the geometry. All

the rectangular blocks have their local structured mesh, which in turn is connected to the surrounding blocks' mesh appropriately. This means that two consecutive blocks will have the same number of nodes in the edge they share, and the opposite edges to that one shared will have the same number of nodes as well, as every local mesh is structured.

Different designs have been tried, given the complexity of the geometry of study. The feedback channels' shape significantly complicates the block distribution in this case. The main difficulty lies in the 4 corners of the feedback channels. With the typical approach, a vertex of a block always falls on the round part of the feedback channels with an angle much higher than 90 degrees, which causes extremely skewed cells.

This can be avoided with an alternative that has finally been discarded because, although it solved the problem on the round edges of the feedback channel, it introduced worse problems in other regions of the mesh. The initial step of the blocking technique consists on creating a single block that contains the whole geometry. Then, this block is split into smaller blocks and these are associated to their corresponding edges of the geometry. This alternative associates the top edge of the initial block (highlighted in red in figure 6.2) to all the top curves (highlighted in bold black in figure 6.3) so that the block distribution in the feedback channel is like the one shown in figure 6.4. With this technique, the mesh in the feedback channels would be very good but it would generate a split of cells in the inlet of the mixing chamber that destroys the mesh uniformity and a general bad block distribution in the rest of the mesh.

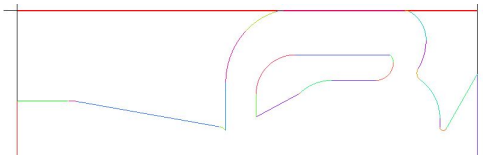

FIGURE 6.2: Detail of the top edge of the initial block highlighted in red

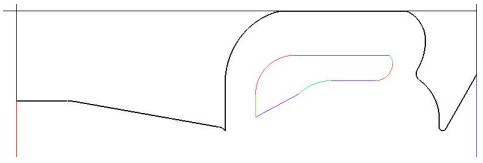

FIGURE 6.3: Detail of the set of all the top curves of the geometry highlighted with a thicker line

Regarding this fact, this alternative has been discarded in favour of the typical approach. This definitive blocking strategy chosen is shown in figure 6.5.

Feedback channels have, in fact, a special type of blocks: o-grids. At first, normal blocks have been created and distributed along the fluidic oscillator. Nevertheless, some of the resulting blocks had a poor shape, being some of them almost triangular (one of the 4 angles was almost 180^{o}), like the one shown in figure 6.6. Then, the mesh has also very poor quality in the critical vertex, as the cells are extremely skew (figure 6.7).

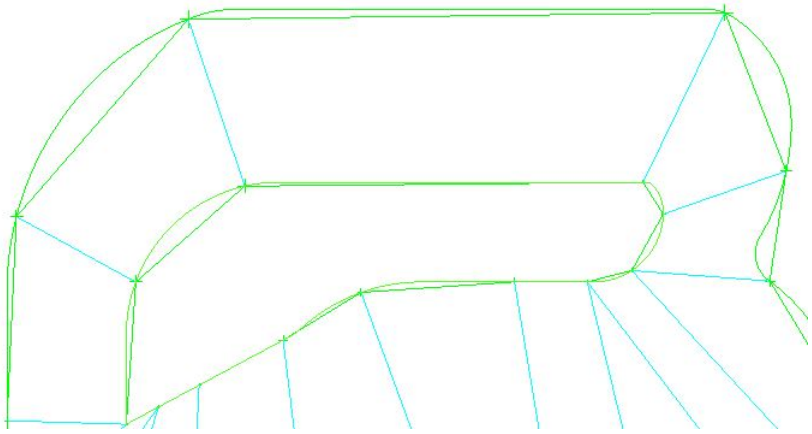

FIGURE 6.4: Detail of the feedback channel blocking alternative in the feedback channels

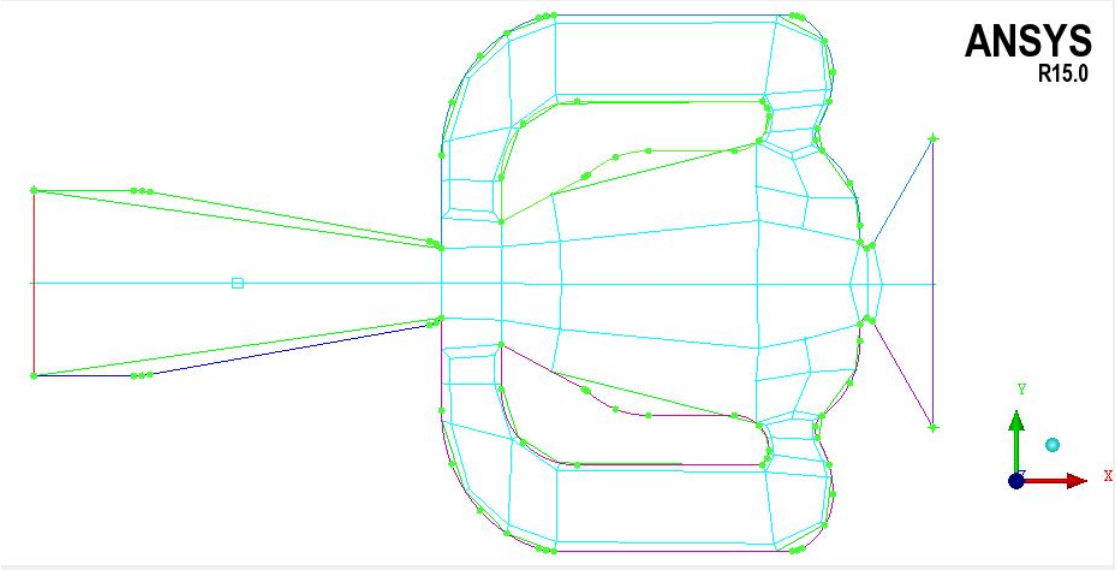

FIGURE 6.5: Definitive mesh blocking strategy with ICEM-CFD

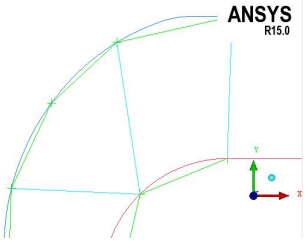

FIGURE 6.6: Block with bad shape caused by the multiple curves of the geometry

In regards of this, an o-grid is used for the problematic blocks. The o-grid allows an improvement of those critical regions, as it transforms the usual rectangular block into a smaller rectangular block surrounded by 4 additional rectangular blocks, each one of them on an edge of the center block (see figure 6.8). The application of this on curves allows a better adaptation of the mesh.

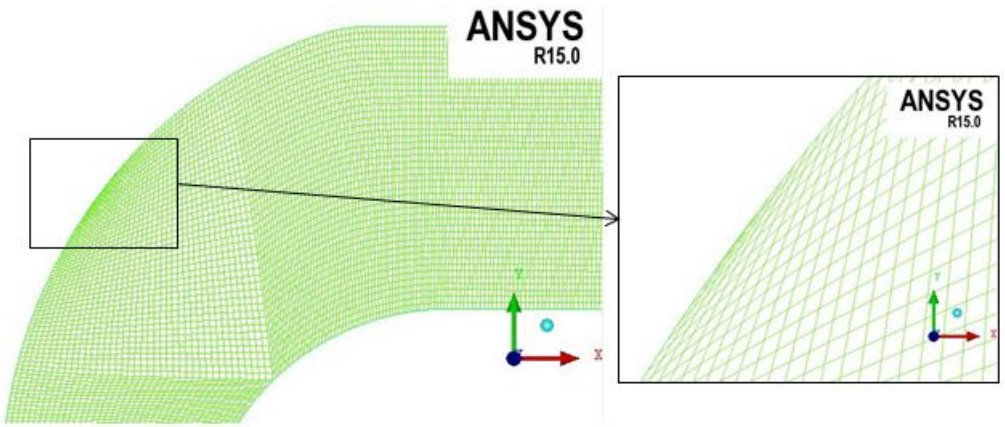

FIGURE 6.7: Poor mesh quality with extreme skewness in the critical vertex as seen in the detail

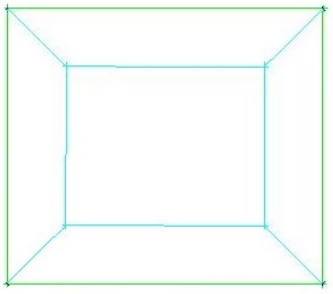

FIGURE 6.8: O-grid block inside a rectangle

At first, o-grids were only used in the 4 critical blocks of the two feedback channels, one at each corner. Nevertheless, this design had an important drawback. The o-grid block is surrounded by 4 other small blocks. When meshing the boundary layer, there must be a significant accumulation of cells near the walls. Then, the 4 small surrounding blocks would have a bigger accumulation of cells than the rest of the blocks of the feedback channel, given that some of them would be near the wall and they would need small cell spacing for the boundary layer representation. The problem is that the rest of these surrounding blocks would be placed perpendicularly to the flow direction, like the other normal blocks, but they would have a different cell spacing than the normal blocks. This, in turn, would create a disturbance in the mesh uniformity in an already complex region, so the mesh quality would be negatively affected.

Then, o-grids have finally been placed all along the feedback channels so that no problems were found in its critical curves, while the rest of the geometry could be well meshed without the use of o-grid blocks. A detail of the critical region where o-grids are specially useful is shown in figure 6.9. It is clear that the mesh quality has been significantly improved with respect to the previous mesh shown in figure 6.7, having much less skewness in the vertex of the block. As a result of the new o-grid blocks distribution, the

disturbance caused by the accumulation of cells due to the o-grid blocking is moved to the feedback channel inlet and outlet, which is less disturbing for the mesh regularity. As said before, the use of o-grids in the feedback channels has a secondary benefitial effect. It allows an easier meshing of the boundary layer in the totality of the feedback channels, given that the external blocks of the o-grid can be placed close to the walls and they can be meshed independently of the central blocks (only in the perpendicular direction of the flow, which is actually the interesting direction as explained before). Therefore, great accumulation of cells near the wall can be done.

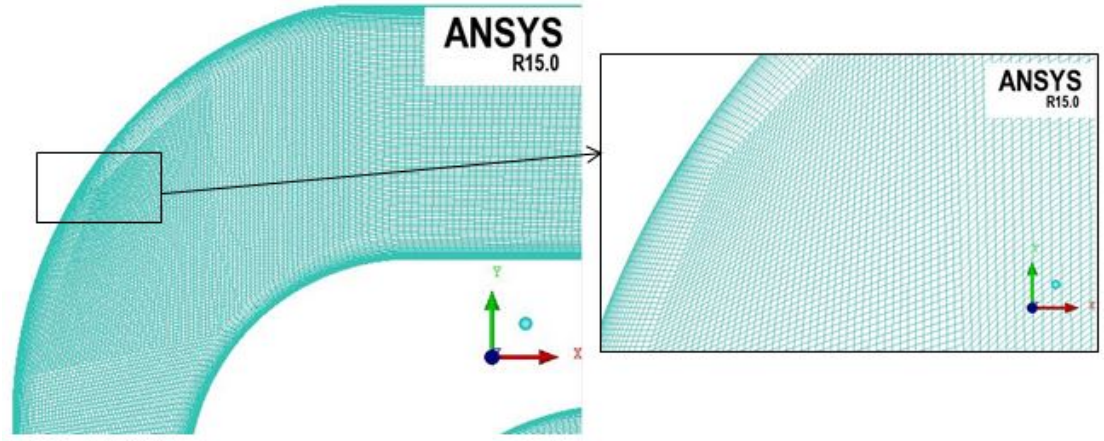

FIGURE 6.9: Improved mesh quality with o-grid application on feedback channels and better boundary layer meshing

Once the blocking strategy is completely defined, an auto-meshing is used as an initial approach. Then, this mesh has to be properly modified so that the distribution is improved focusing on all the different regions and details of the mesh, considering the criteria for a good mesh. That means that many edges of many blocks have to be manually modified. These modifications include redefinition of nodes' distribution along an edge. For example an exponential law for the distribution of cells near the wall in order to accumulate them in one side, or a specific new law that enables a smooth change of cells' size along a block in order to avoid big size differences between consecutive cells. Of course, changing the edge of one block might automatically change contiguous blocks' edges because the global mesh needs to be always structured, so a balanced combination must be found.

Three different meshes have been finally designed with different levels of density, so that an independence mesh test can be performed. With this test it is possible to verify if the mesh density is enough or if denser meshes are required for higher accuracy. The three meshes have 166000, 195000 and 370000 nodes. The 195000 nodes mesh has been built from the 166000 nodes mesh by adapting some specific regions of the mesh, trying to increase its quality and regularity. The number of nodes in the walls of the mixing

chambers and in the feedback channels have been slightly increased in order to have higher precision in those critical regions. Moreover, the number of nodes in the outlet have also been increased in the direction of the flow. The 370000 nodes mesh is simply a proportional densification of the 166000 nodes mesh, using an ICEM tool that performs this densification automatically. Details of the mesh of 166000 nodes are shown below.

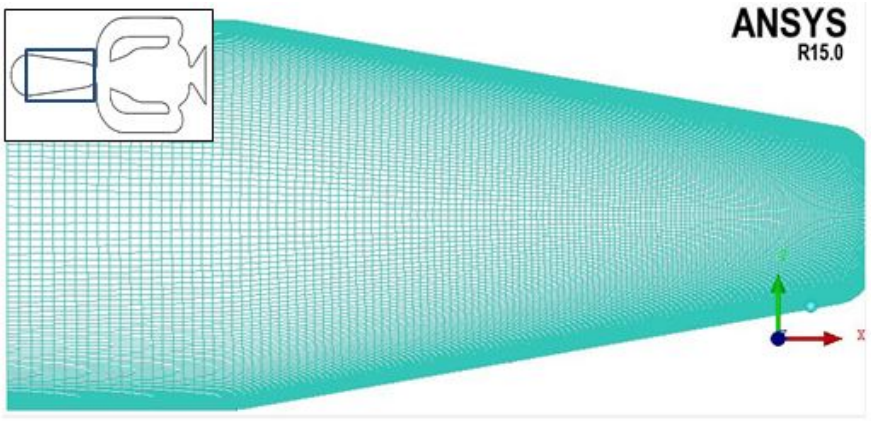

FIGURE 6.10: Inlet detail

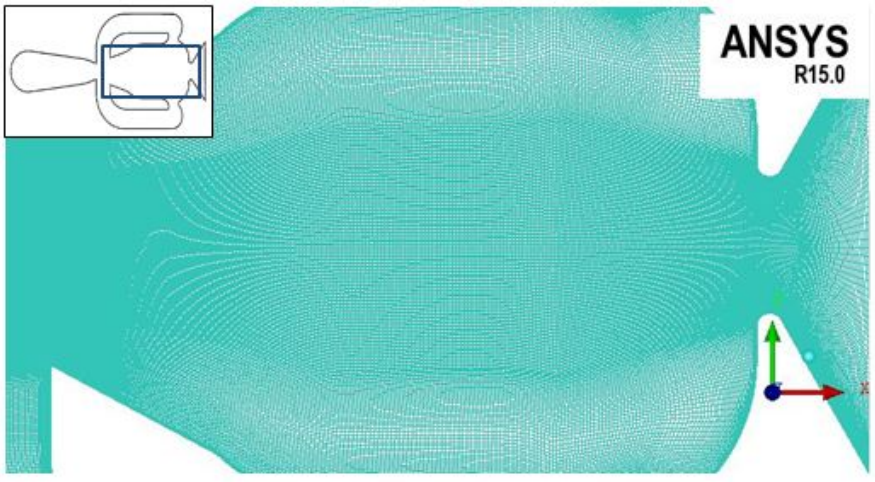

FIGURE 6.11: Mixing chamber detail

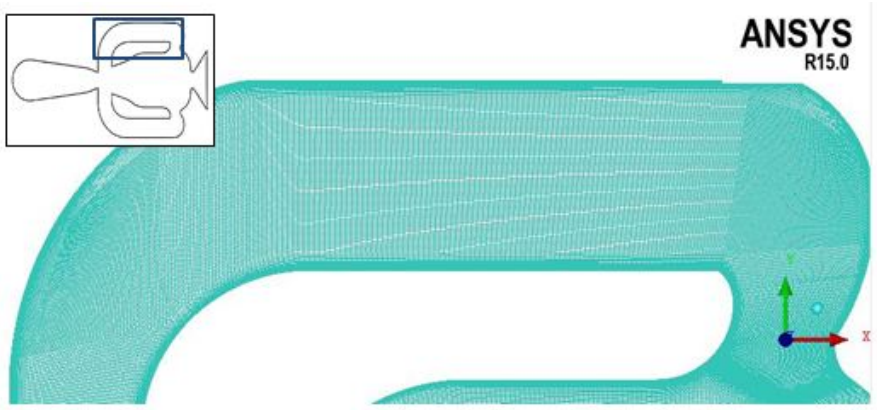

FIGURE 6.12: Top feedback channel detail

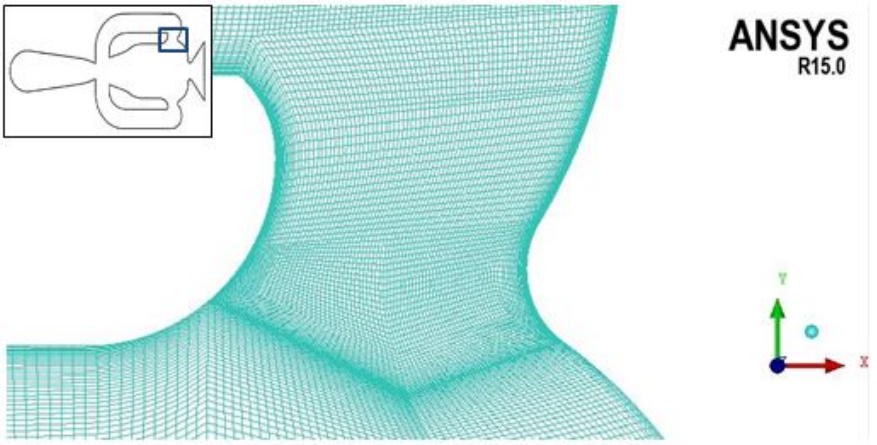

FIGURE 6.13: Inlet of the top feedback channel detail

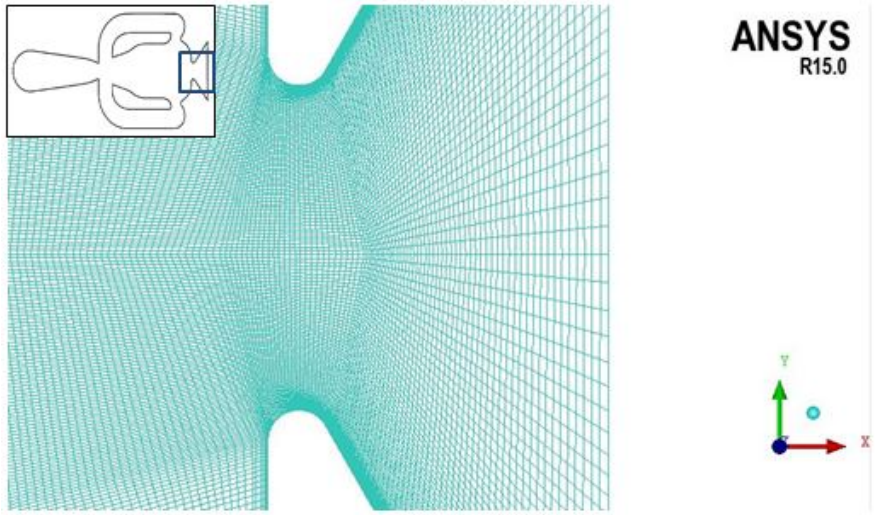

FIGURE 6.14: Outlet detail

6.3 Mesh independence test

The mesh is an important element of a good numerical analysis. In order to verify that the mesh is not a source of error, a mesh independence test must be performed. Different meshes with different levels of density are used and the corresponding results are compared. The mesh quality is acceptable when the use of a finer mesh does not provide any change in the results. As said before, three meshes are used: one with 166000 nodes, one with 195000 nodes and one with 370000 nodes. Regarding the study by Ruiz [8], where his finest mesh of 210000 nodes took more than 3 days to calculate a few cycles, the computations with the designed meshes are likely to extend significantly over time. Indeed, table 6.1 shows the frequencies obtained and time needed by each mesh to compute between 5 and 10 cycles of oscillation:

	Coarse mesh	Medium mesh	Fine mesh
Number of nodes	166000	195000	370000
Frequency	3049 Hz	3050 Hz	3025 Hz
Computing time	4 days 21 h	5 days 6 h	10 days 13 h

TABLE 6.1: Frequencies and time requirements of each mesh

It is important to highlight that given the large time requirements, the results for the finer mesh do not correspond to a fully stable flow. More time steps would be necessary to reach a completely stabilised flow so that the frequency is more accurate. Figure 6.15 shows the superposition of the flow for the coarse and the medium mesh. The finer mesh has not been included owing to the fact that it did not have a stable enough oscillation yet.

Figure 6.15 illustrates that the differences between the results obtained from the medium and the coarse mesh are minimal and can be neglected. Considering this and the fact that the coarse mesh requires significantly less time to perform the simulation, it is clear that the coarse mesh is the best one for the scope of this project. However, future studies that require less preliminary work to the simulations could use finer meshes in order to achieve more accuracy in the results. Of course, the fine mesh is not useful for this oscillator regarding the fact that it duplicates the time requirements and the memory space for the simulation whereas it would not provide more accuracy.

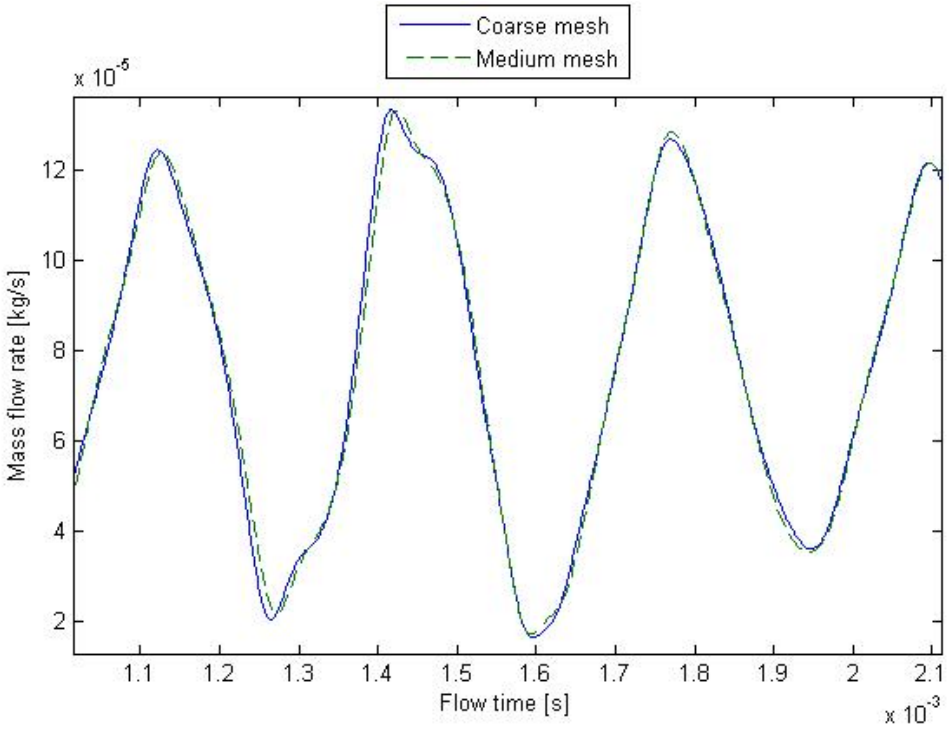

FIGURE 6.15: Mass flow rate on the lower outlet for the coarse and the medium mesh

6.4 Simulation

The numerical simulation has been performed with ANSYS Fluent software. As in the previous studies in ETSEIAT [8, 17], it is a bidimensional study, given that 3D meshes are excessively large and involve too long calculations beyond the scope of this project.

6.4.1 Phases of the simulation

The simulation is expensive in terms of time. Therefore, a special procedure has been followed in order to minimise it: initially, a laminar and a turbulent steady-state analyses have been performed for a few iterations for the simplest mesh, which is much less computationally expensive; then, the same analyses have been performed for a non-steady-state simulation; finally, the available data has been interpolated for the denser meshes and the turbulent non-steady-state simulations have been done for these meshes. Hence, a lot of time can be saved, given that the complex analyses start from a real case or, at least, a flow field that is much more similar to the real case than the usual simple initialisation solutions, and a lot of slow iterations can be omitted. In addition, it is interesting to analyse the flow under laminar conditions, given that the Reynolds number

is in the verge between laminar and turbulent flow and not much is known about the behaviour of fluidic oscillators under these conditions.

6.4.2 Configuration

The inlet gauge pressures range between 10 kPa and 165.47 kPa, according to the experimental analysis by Raghu [1]. Through the continuity equation

$$\dot{m} = \rho v A \tag{6.1}$$

and knowing the mass flux for some inlet pressures (see table 4.2), an estimated inlet speed can be obtained (density is considered at sea level). Thus, the inlet velocity ranges from 27.80 m/s to 1246.32 m/s and the Reynolds number ranges respectively from 2881 to 129202. Regarding this fact, the flow can be assumed as turbulent, given that the usual Reynolds critical number is about 3000 in ducts.

Apart from this, it is important to remark the fact that the analysis is performed under the hypothesis of incompressible flow. The reason for an incompressible analysis is simple: time requirements are increased for compressible flow studies, since more equations have to be accounted for. This hypothesis can be assumed for a limited interval of speeds, given that air at high speeds must be considered as a compressible fluid. The limitation is found through the Mach number, defined as $M = \frac{a}{a_0}$ where a represents the air local speed and a_0 the sound speed in air. Sound speed at the conditions of the analysis (ambient temperature $T = 293$ K) is $a_0 = \sqrt{\gamma RT} = 343.11$ m/s and the limiting Mach number is usually set around 0.30. For this study, a maximum inlet gauge pressure level is set at 20 kPa, given that for this pressure the maximum Mach number in the oscillator is $M = 0.34$, which is still acceptable and thus the range of study changes from an inlet gauge pressure of 10 kPa to 20 kPa. The maximum inlet speed for this range is $a = 44.84$ m/s, which corresponds to an inlet Mach number $M = 0.13$. Hence, the maximum Reynolds and the maximum mass flux can be also computed: $Re = 4637$ and $\dot{m} = 2 \cdot 10^{-4}$ kg/s.

In chapter 5 all the theory and justifications behind the numerical parameters are explained. Hence, the following parameters have been set. As suggested by Ruiz [8], the solver used here is pressure-based, given that the velocity is low and the flow can be considered as incompressible. The SIMPLE scheme is chosen due to its simplicity. Convergence is easier with small time steps but the computational costs may be excessive then, since a lot of time steps are required for only small time advancements. The order of magnitude of the time step size is set around 10^{-7} and 10^{-6} s, so that convergence

can be reached. The number of time steps is such that a few cycles of oscillation are analysed, considering that the first cycles will not be usable for not having reached convergence yet. As suggested by Ruiz [8], the convergence criteria is established at 10^{-5} for all the equations. Finally, as said in chapter 5 and according to Ruiz [8] and Bobusch et al. [12], the $k-\omega$ SST turbulence model is also used.

Apart from that, the boundary conditions and the fluid used need to be also set. As mentioned in chapter 4 and in a previous paragraph, inlet conditions are based on pressure, while the outlet is supposed to be at ambient pressure. The air is assumed to have its constant properties at sea level (see table 6.2). Additional parameters must be set for the inlet and the outlet for the turbulence model: turbulent intensity and hydraulic diameter. Turbulent intensity is defined as:

$$I = \frac{\sqrt{\overline{v'^2}}}{\bar{v}} \tag{6.2}$$

As suggested by Ruiz [8] it is set at a 5%. The hydraulic diameter is defined as:

$$D = \frac{4A}{P} \tag{6.3}$$

Where A stands for the area and P for the perimeter of the duct (see table 6.2 for the hydraulic diameters of the fluidic oscillator of study). Finally, the walls need to have their own boundary conditions. The required parameters are a shear condition, which is set to "no slip" (remember the viscous boundary layer that must satisfy this boundary condition in the wall), and a roughness constant, which is left at the default value of 0.5. The conditions set for the simulation are finally summarised in table 6.2:

6.4.3 Data monitoring

The final step of the simulation is the post-processing of results. In order to obtain results, monitors are required. Monitors are the equivalent of sensors in experimental studies. A monitor can be a point, a line or a surface. In this study, the main goal is to obtain the frequency of oscillation of the exiting flow of the device. This is why the outlet line contains three mass flux monitors: one is placed along the whole length of the outlet vertical line and is in charge of measuring the total mass flux of the outlet, which obviously is the same as the inlet mass flux and should correspond to the experimental mass flux; the other two sensors divide the outlet into two halves, an upper one and a lower one, so that the oscillation can be captured. The sum of the last two monitors must be always the same and equal to the total mass flux that the first monitor measures,

Solver	Pressure-based		
Time	Transient		
Dimensions	2D		
Model	Viscous SST $k-\omega$		
Fluid	Air	Density	1.225 kg/m^3
		Viscosity	$1.789 \cdot 10^{-5}$ kg/(m·s)
Boundary conditions	Inlet	Gauge total pressure	$10-20$ kPa
		Turbulent intensity	5.00%
		Hydraulic diameter	0.00151 m
	Outlet	Gauge total pressure	0 kPa
		Backflow turbulent intensity	5.00%
		Backflow hydraulic diameter	0.00163 m
	Walls	Shear condition	No slip
		Roughness constant	0.5
Solution Methods	Scheme	SIMPLE	
	Spatial Discretisation	First Order Upwind	Turbulent Kinetic Energy and Specific Dissipation Rate
		Second Order	Pressure and Momentum
Time step	Size (s)	Order of magnitude between 10^{-7} and 10^{-6}	
Convergence criteria	Absolute. 10^{-5} for all the equations.		

TABLE 6.2: Main simulation settings on Fluent

and while one of them has a higher mass flux, the other one is proportionally reduced (representing the majority of air exiting with a certain angle at the outlet depending on time). In addition, mass flux and pressure monitors have been placed in the centre, inlet and outlet of the feedback channels as well.

Chapter 7

Results

In this chapter, the results found for the cases of study are presented. First, the steady-state simulation is analysed in section 7.1. Only a preliminary analysis is performed given that this simulation is only done in order to provide the non-steady-state simulations with a first solution similar to the real one. Thus, much time can be saved. In section 7.2 the non-steady-state simulations are analysed. The outlet flow frequency is studied in front of the inlet gauge pressure and the inlet velocity, and the flow of the fluidic oscillator is characterised. In addition, a laminar simulation is performed in order to evaluate a low Reynolds flow under laminar conditions.

It is important to clarify an aspect about the images of the velocity and pressure fields provided in this chapter. They are only used as a support for the discussion of results. Their only function is to visualise the flow qualitatively in order to have an idea of how the flow evolves inside the oscillator and to understand the reason for the exiting oscillation. A legend is obviously attached to the image but the specific values of velocity and pressure are not important to the discussion of the results.

7.1 Steady-state analysis

The steady state analysis is not likely to provide good results, given the time-dependent nature of the fluidic oscillator. However, it is really useful for a first analysis, which does not represent an exact solution but provides a much more similar flow to the real one. Hence, it is a better starting point than the Fluent solution initialisation for the non-steady-state simulations, which in turn are much slower.

The laminar analysis has not provided good results. After 1000 iterations (a 20 minutes simulation on a PC equipped with an Intel i5 processor at 2.4 GHz with a 4GB RAM

memory), the residuals show a clear stabilisation far from convergence and the resulting flow only slightly resembles the expected field.

A turbulent analysis has been performed then, starting from the previous laminar results. 1000 more iterations have been done and the velocity field obtained is much more similar to the expected results. Convergence has not been reached: the residuals oscillate randomly around an order of magnitude of 1 for the continuity equation and 10^{-3} for the rest of equations. Nevertheless, this is reasonable, because the non-steady nature of the fluidic oscillator does not allow convergence to be reached for a steady-state analysis. Table 7.1 shows the numerical values obtained and the experimental data while figure 7.1 shows the resulting velocity field obtained by the steady-state turbulent analysis.

	Experimental	Numerical
Inlet velocity	27.80 m/s	36.60 m/s
Mass flow rate	$1.18 \cdot 10^{-4}$ kg/s	$1.59 \cdot 10^{-4}$ kg/s

TABLE 7.1: Experimental and numerical values for an inlet gauge pressure of 10 kPa

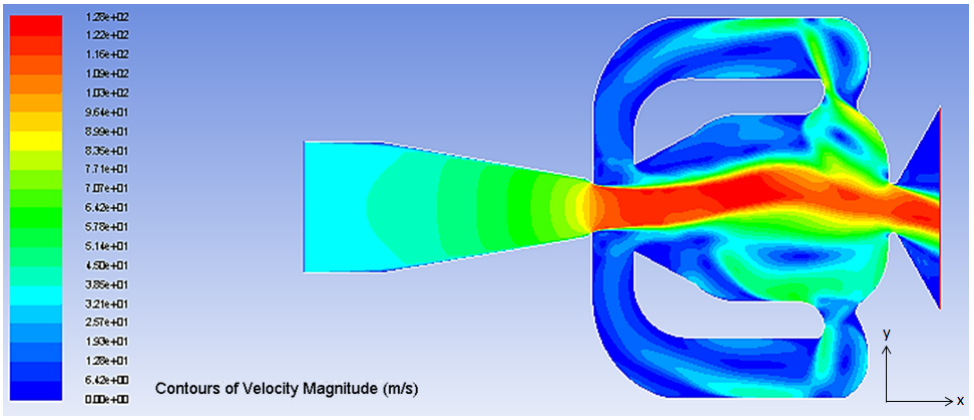

FIGURE 7.1: Velocity magnitude field at 10 kPa inlet gauge pressure

Figure 7.1 shows a specific instant of the time-dependent behaviour of the oscillator, given that the analysis is being performed under steady-state conditions. It is at a phase between 0 and 180 degrees, with the main jet being deflected towards one of the two walls. The flow characteristics are qualitatively illustrated here. The two recirculation bubbles can be easily identified next to the walls of the mixing chamber, although they seem to be moved significantly to the downstream part of the mixing chamber. This fact needs to be analysed later with the non-steady-state simulation. At the same time, a flow is being generated in the top recirculator that will soon change the wall attachment to the other side of the oscillator.

7.2 Non-steady-state analysis

7.2.1 Laminar

As seen in chapter 6, the Reynolds number is very low for the lowest inlet gauge pressure conditions. Therefore, a laminar non-steady-state analysis is performed in order to see if under pure laminar conditions the fluidic oscillator is capable of oscillating. The convergence of the residuals of this simulation has been extremely difficult with a time step of $2.5 \cdot 10^{-6}$ s, unless smaller time steps were used (although in this case the simulation would take too long for the present work). A reason for the difficulty for convergence might be that the Reynolds number is not low enough for the laminar analysis to correctly simulate the flow conditions, since turbulence might still have an influence. Nonetheless, the oscillator has provided an oscillatory flow. This flow has an approximately constant frequency of oscillation but does not show a clear periodic pattern repeated for each cycle. It has not been possible to obtain a stable flow using the laminar simulation. Moreover, the frequency of oscillation (around 3300 Hz) is far from the experimental one (400 Hz). Table 7.2 shows the numerical values obtained and the experimental data, while in figure 7.2 the mass flow rate through inlet and the top and lower halves of the outlet is shown.

	Experimental	Numerical
Inlet velocity	27.80 m/s	28.57 m/s
Mass flow rate	$1.18 \cdot 10^{-4}$ kg/s	$1.24 \cdot 10^{-4}$ kg/s

TABLE 7.2: Experimental and numerical values for an inlet gauge pressure of 10 kPa

Figure 7.2 shows that the oscillator has a gain, since there is a backflow current in one of the outlets while the other one provides a higher mass flux than the inlet.

Apart from that, Ruiz [8] also performed a laminar analysis of his oscillator but at higher Reynolds numbers, and he did not obtain any oscillation. In regards of figure 7.2, an oscillation appears for laminar flow if low Reynolds numbers are used, although it does not seem to be stable since it does not follow the same pattern at each cycle. As said before, this can be caused by the fact that the Reynolds number is in the limit between turbulent and laminar conditions. It could also be due to an excessively large time step that hinders convergence and induces an unstable flow and a misleading frequency. In conclusion, given that the oscillation obtained is not stable, the laminar simulation cannot be used for the range of analysis studied here.

A possible study for future works would be to analyse the flow with lower Reynolds numbers under laminar conditions. This could lead to clearer oscillations and maybe

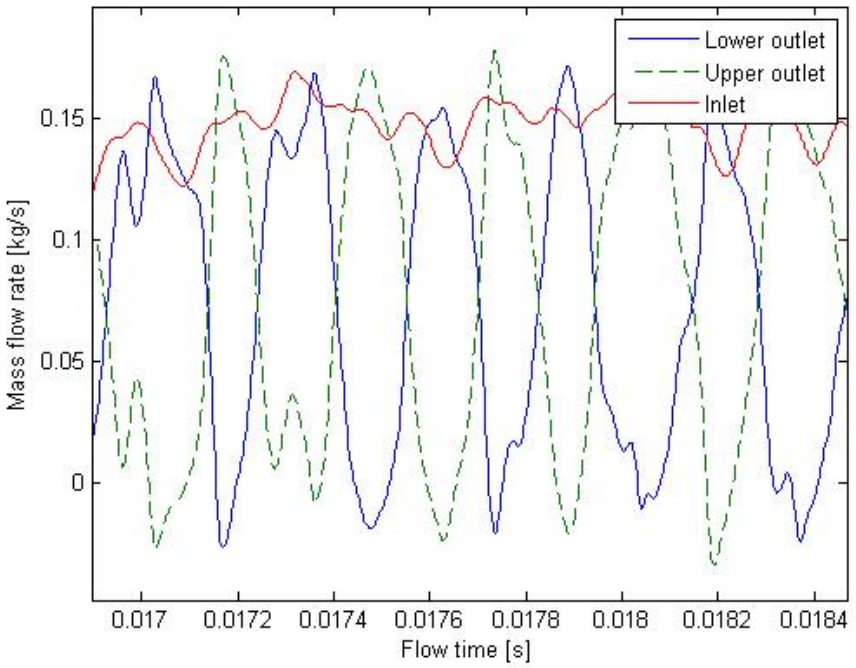

FIGURE 7.2: Inlet and top and lower outlets mass flow rate for inlet gauge pressure of 10 kPa and laminar conditions

interesting changes in the oscillation features, such as the frequency. In addition, a lower time step would facilitate the calculations, but much more time would be needed then.

7.2.2 Turbulent

Owing to the fact that the laminar analysis does not provide results to compare with the experimental data, a turbulent analysis is performed, using the $k-\omega$ SST model. This kind of analysis introduces equations to consider the turbulence effects and it should provide more accurate results. The analysis of the oscillator for an inlet gauge pressure of 10 kPa and a time step at 10^{-6} s shows a periodic oscillatory flow, as seen in figure 7.3, while in table 7.3 the numerical and experimental mass flux and inlet velocity are compared.

	Experimental	Numerical
Inlet velocity	27.80 m/s	35.48 m/s
Mass flow rate	$1.18 \cdot 10^{-4}$ kg/s	$1.54 \cdot 10^{-4}$ kg/s

TABLE 7.3: Experimental and numerical values for an inlet gauge pressure of 10 kPa

Figure 7.3 includes the inlet mass flow rate, which facilitates the observation of the frequencies involved in the oscillation, and it appears to be oscillating as well. It is important to remember that the boundary condition for the present study is the inlet

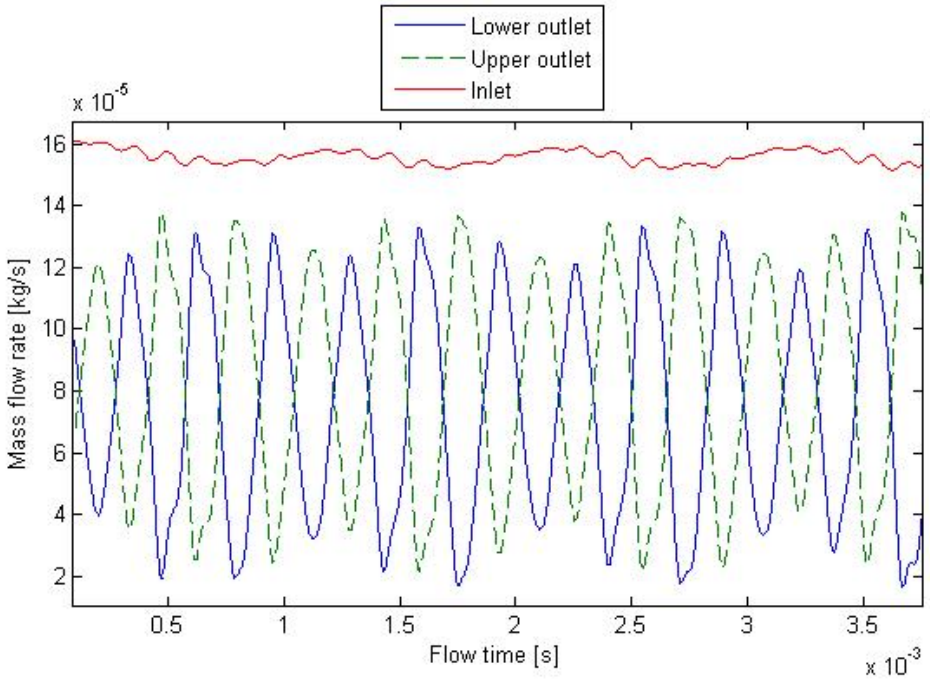

FIGURE 7.3: Inlet and top and lower outlets mass flow rate for inlet gauge pressure of 10 kPa, time step at 10^{-6} s and turbulent conditions

pressure, not the inlet mass flow rate. The frequency of oscillation of the inlet mass flux is of 1047 Hz, while the exiting flow oscillates around Y axis at 3049 Hz. However, the inlet mass flux fluctuations are really small and do not need to be considered for the frequency study. They are only useful to explain the fluctuations of the amplitude of oscillation of the outlet mass fluxes.

The frequency of oscillation is 3049 Hz in front of the experimental frequency of 400 Hz. This is a considerable difference but is still in accordance with the frequencies found for the rest of the study, as they all seem to agree in the fact that the frequency of oscillation for an inlet gauge pressure of 10 kPa is around 3000 Hz.

A possible cause for the difference in results might be in the fact that the study is performed under incompressible conditions. Gases are compressible but, as said before, if the gas Mach number is low enough, compressibility effects can be neglected. However, there are considerable velocity changes along the fluidic oscillator. While the inlet has a Mach number of $M = 0.1$, other parts of the flow can reach $M = 0.3$, which is the usual limit for incompressible flow. Thus, there might be an important effect due to compressibility that is not being considered in the present analysis and this might cause the erroneous result. Besides, the compressibility of the fluid might be also a cause for small differences in the results shown in table 7.3.

Another possibility might be due to the use of excessively large time steps that could entail misleading frequencies, as seen here. In spite of that fact, the time requirements

for small time steps are beyond the scope of this project. In addition, the use of a First Order discretisation might not be precise enough and introduce additional error sources.

Finally, there is another possible error source: the geometry. It is possible that the geometry provided in the paper by Raghu [1] is distorted in some way and that, in reality, the geometry used in the present work is not exactly the same as the experimental geometry. This is likely to be the answer for such difference in the frequency of oscillation. Considerations about compressibility, time steps and spatial discretisation definitely have an impact on the resulting frequency but it is improbable that they justify such a big difference. Moreover, the differences between the numerical and the experimental mass fluxes shown in table 7.3 support this idea, because a given inlet pressure at a specified area should provide a specific mass flow rate. Anyway, if following studies verified the present results, they could be considered correct for the geometry used in the present study, independently from the real geometry studied by Raghu.

7.2.3 Frequency study

The flow has been analysed for a range of inlet gauge pressures between 10 kPa and 20 kPa. It is a limited range in comparison with the experimental range studied by Raghu [1], but considering the incompressibility hypothesis assumed in the present work, the analysis of the oscillator under higher inlet pressures would introduce an error in the results.

The study of the outlet mass flow rate provides the frequency of oscillation of the exiting jet. Table 7.4 shows the frequency of oscillation of the exiting jet for the specified range of inlet pressures and their corresponding inlet velocities. The inlet velocity has been obtained through the mass flow rate monitor and the continuity equation.

Inlet gauge pressure [kPa]	**Inlet velocity [m/s]**	**Frequency [Hz]**
10	29.98	3049
12.5	38.88	3497
15	44.11	3812
17.5	49.49	4095
20	56.86	4401

TABLE 7.4: Frequency of oscillation of the exiting jet for each boundary condition of the range of study

Figure 7.4 and 7.5 illustrate the frequency of oscillation of the exiting jet in front of the inlet gauge pressure for the numerical analysis and the experimental study respectively.

As seen by comparison between figures 7.4 and 7.5, the range of study of the numerical analysis is very limited and clearly far from the experimental results. However, as said

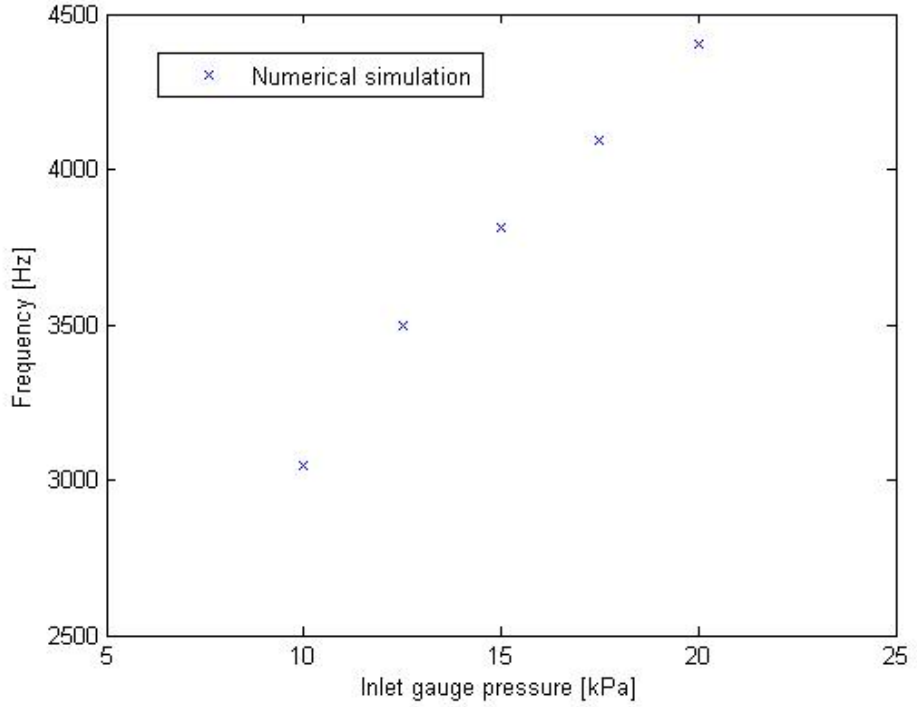

FIGURE 7.4: Frequency of oscillation of the exiting jet versus inlet gauge pressure

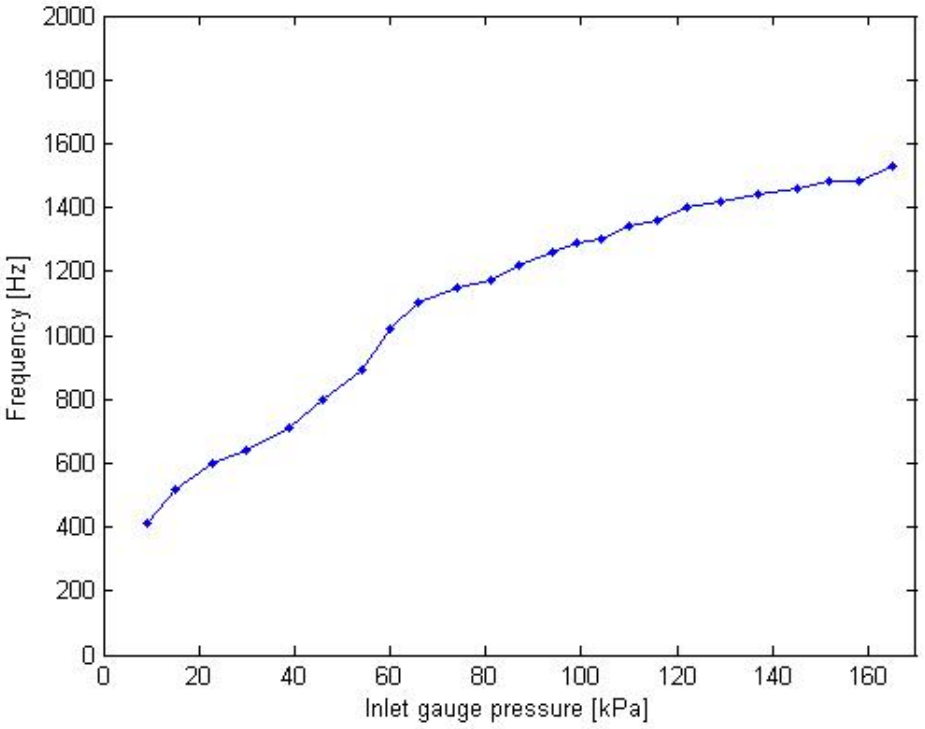

FIGURE 7.5: Experimental frequency of oscillation of the exiting jet versus inlet gauge pressure [1]

before, the possibility of having used a different geometry for the present work than in the experimental study due to lack of data is likely to be the reason for this difference. Apart from that, both figures seem to show a similar curvature between frequency and inlet gauge pressure in the range of study.

In figure 7.6 the frequency of oscillation of the exiting jet is represented with respect to the inlet velocity and a linear regression of the values is shown.

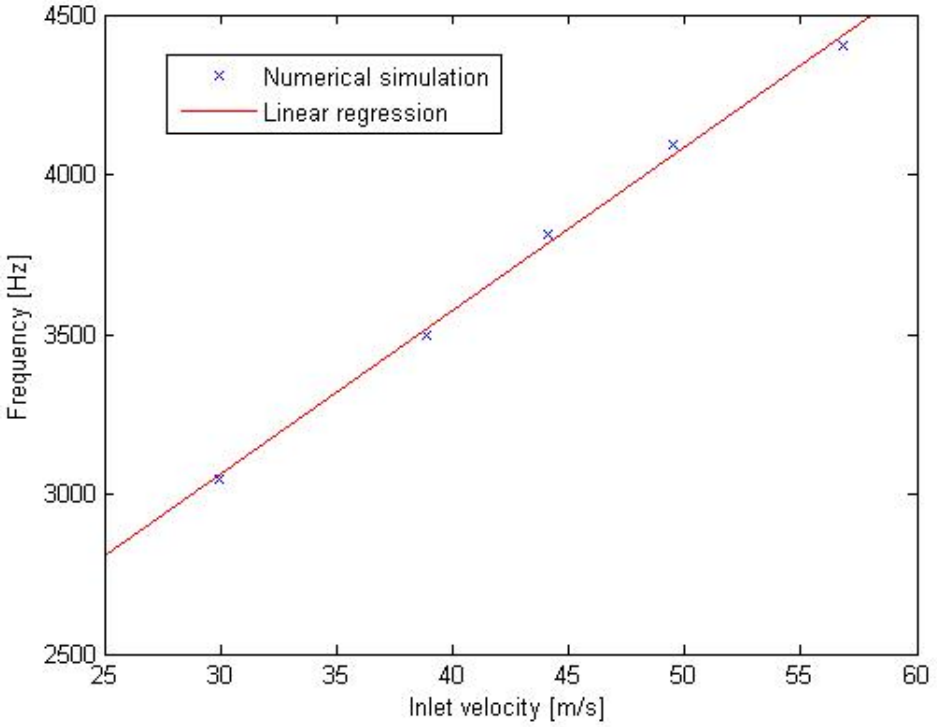

FIGURE 7.6: Frequency of oscillation of the exiting jet versus inlet velocity

It can be seen that the frequency of oscillation tends to follow a linear trend with respect to the inlet velocity, even for the highest pressures of study that are near the compressible region. This agrees with previous results obtained by Ruiz [8].

7.3 Flow characterisation

In this section the main aspects of the flow are analysed, in order to understand the features that define the oscillation of the fluidic oscillators. As said in the introduction of this chapter, the figures of the velocity and pressure fiels are only used as a support for the discussion of the results. They are illustrative of the flow evolution during the cycle but the quantitative values of pressure and velocity are not analysed with this figures, but with graphics provided in other sections.

7.3.1 Phases of the oscillation

Each phase of the oscillation must be clearly characterised. In figure 7.7 the oscillator at a phase of 0 degrees is shown. The main jet is attached to the lower wall of the mixing chamber and exits through the upper outlet. At the same time, the lower feedback channel is receiving the input flow from the main jet and starts working.

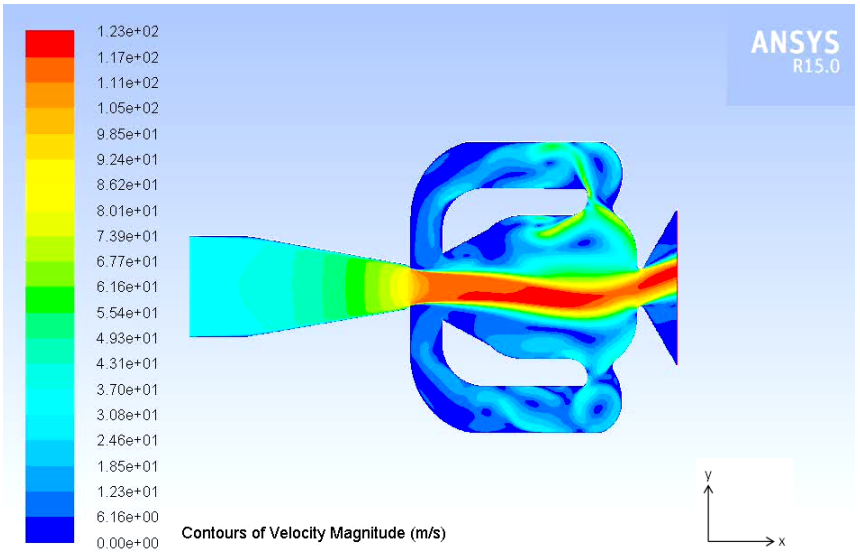

FIGURE 7.7: Velocity field at 0 degrees phase of the oscillation for inlet gauge pressure of 10 kPa

In figure 7.8 the 90 degrees phase is shown. The main jet is transitioning to the upper wall of the mixing chamber and exiting in a straight line. The lower feedback channel is having its peak flux, while the upper feedback channel is at its lower mass flow rate.

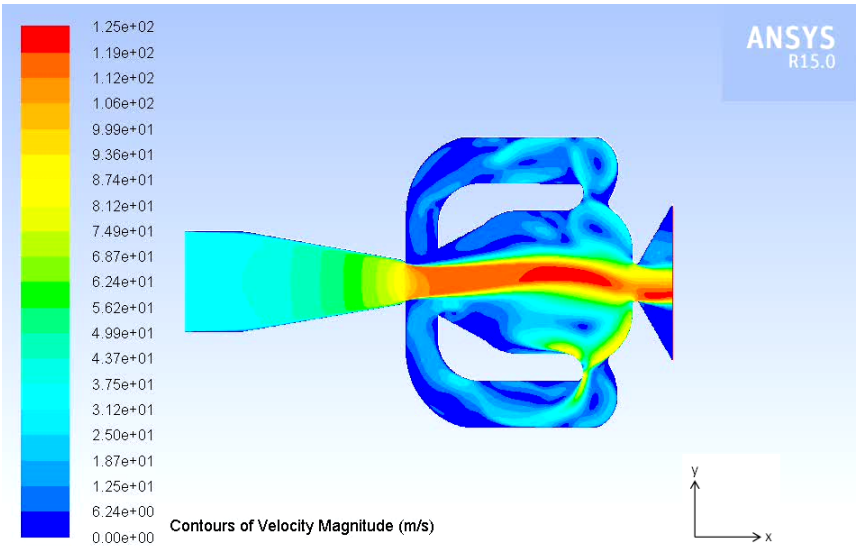

FIGURE 7.8: Velocity field at 90 degrees phase of the oscillation for inlet gauge pressure of 10 kPa

In figure 7.9 the 180 degrees phase is shown. It illustrates the opposite scenario than the 0 degrees phase. The main jet is attached to the upper wall and exits through the lower outlet. At the same time, the upper feedback channel is starting to work while the lower feedback channel is losing strength.

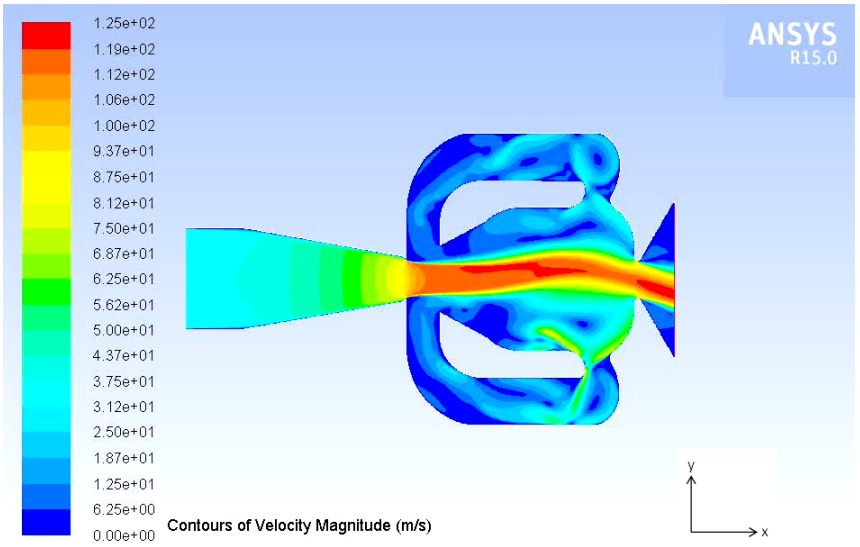

FIGURE 7.9: Velocity field at 180 degrees phase of the oscillation for inlet gauge pressure of 10 kPa

In figure 7.10 the 270 degrees phase is shown. The main jet is transitioning to the lower wall of the mixing chamber because of the upper feedback channel that is supplying its peak mass flux and pushing the main jet to the other side. The exiting jet is straight and the lower feedback channel is providing the minimum mass flux of the whole cycle. The next step would correspond to the 0 degrees phase again, shown in figure 7.7.

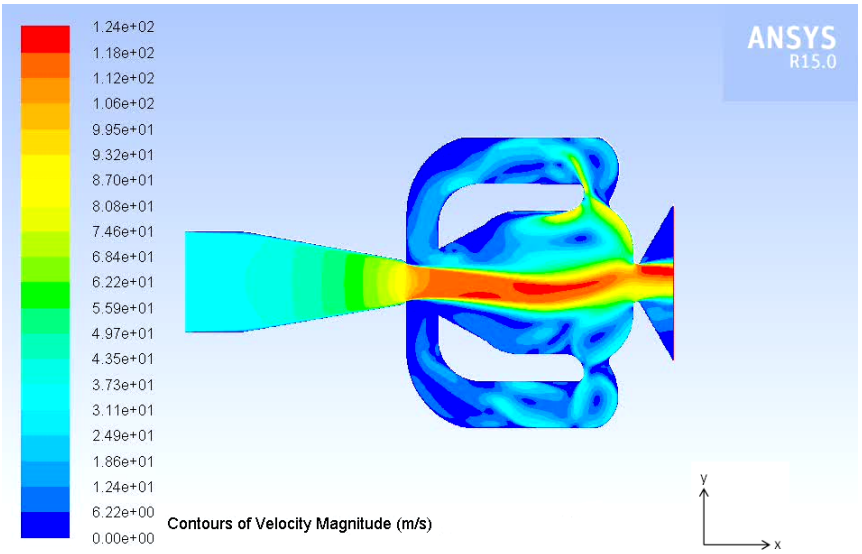

FIGURE 7.10: Velocity field at 270 degrees phase of the oscillation for inlet gauge pressure of 10 kPa

From these figures it is possible to observe that the amplitude of oscillation is small. In fact, from figure 7.7 and figure 7.9 it can be seen that the main jet never attaches completely to the walls of the mixing chamber. The geometry of the end of the mixing chamber does not allow the jet to fully deflect because the pressure gradient would be excessive when it had to move from the wall of the mixing chamber to the outlet. Figure 7.11 illustrates the pressure field of the oscillator for a phase of 0 degrees and it is possible to identify a high pressure region located next to the outlet of the mixing chamber, where the jet bends from the wall to the center of the mixing chamber again at the outlet. Hence, the exiting jet cannot have a big amplitude of oscillation neither.

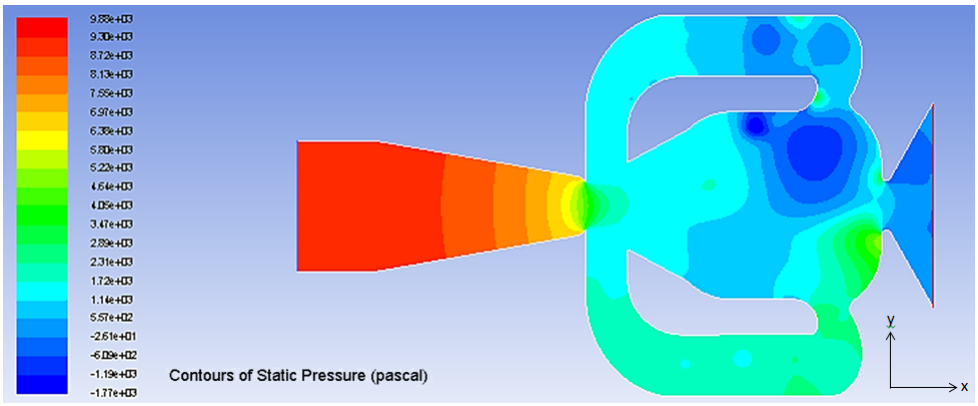

FIGURE 7.11: Pressure field at 0 degrees phase of the oscillation for inlet gauge pressure of 10 kPa

Finally, the recirculation bubbles must be analysed as well. In the turbulent steady-state simulation, recirculation bubbles have been identified but at a very downstream location, at the feedback channels inlets. These bubbles actually exist given that they can be seen in the non-steady-state simulations, such as in figures 7.7, 7.8, 7.9 and 7.10. Figure 7.12 and 7.13 better illustrate the recirculating bubbles on the walls of the mixing chamber at a 90 degrees phase.

In fact, it seems that these bubbles become wider, comprising the whole region between the main jet and the wall of the mixing chamber, when the main jet is moving away from that wall (figure 7.13). Nonetheless, there also seem to be two additional small recirculation bubbles located near the walls of the mixing chamber, in the region where they are usually detected (figure 7.12). They appear when the main jet is in the middle of the mixing chamber and moving towards the same wall where they are located, in the low pressure region, but they disappear when the jet approaches the maximum bending point near the wall. They are difficult to detect but in figures 7.7 and 7.8 they can be seen in the top region of the mixing chamber while in figures 7.9 and 7.10 they can be seen in the lower part of the mixing chamber. It looks like the big bubble splits into two smaller bubbles for a small time when the jet is approaching to the same wall where they are, although the strongest bubble is always at the inlet of the feedback channel.

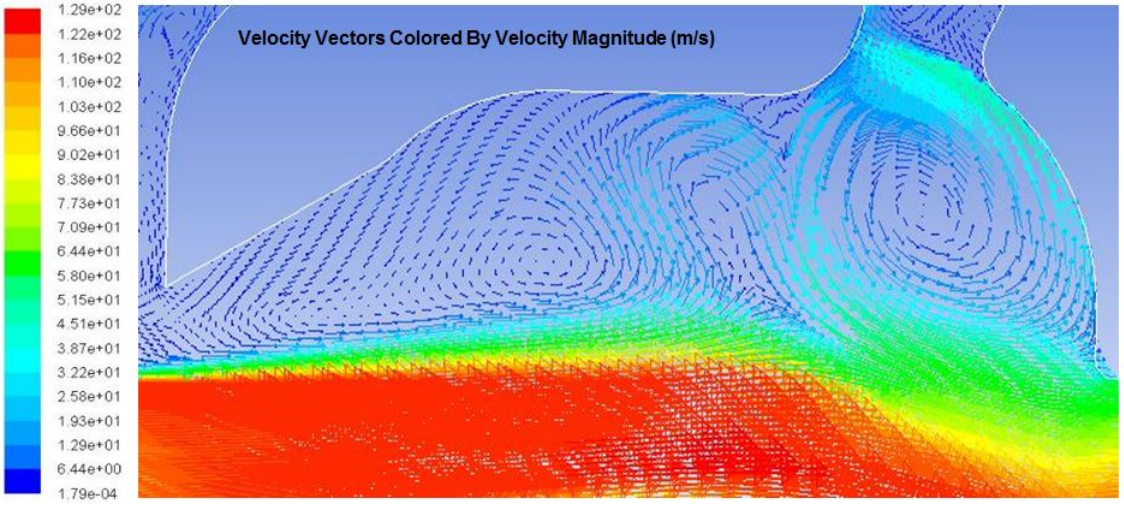

FIGURE 7.12: Velocity vectors in the upper half of the mixing chamber for inlet gauge pressure of 10 kPa

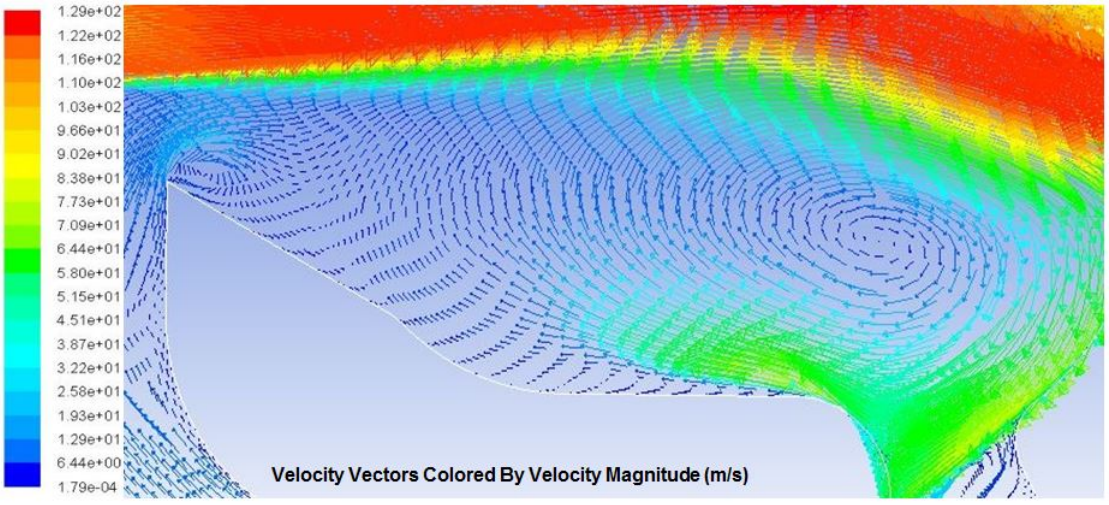

FIGURE 7.13: Velocity vectors in the lower half of the mixing chamber for inlet gauge pressure of 10 kPa

7.3.2 Feedback channels

Feedback channels are the key elements for the oscillation. Therefore, their study is also essential for the understanding of the oscillator. Figure 7.14 shows the mass flow rate for each channel and the sum of the two of them.

It is important to highlight that the oscillation of the total mass flow rate of the two feedback channels is due to the oscillation of the inlet mass flow rate and has no other meaning. Apart from that, the oscillation frequency in the feedback channels is the same as in the outlet. It is reasonable that it is the same given that the recirculating flow through the feedback channels is responsible for the exiting oscillating flow. However, there is no reason why they should be at the same phase as the exiting flow. In order

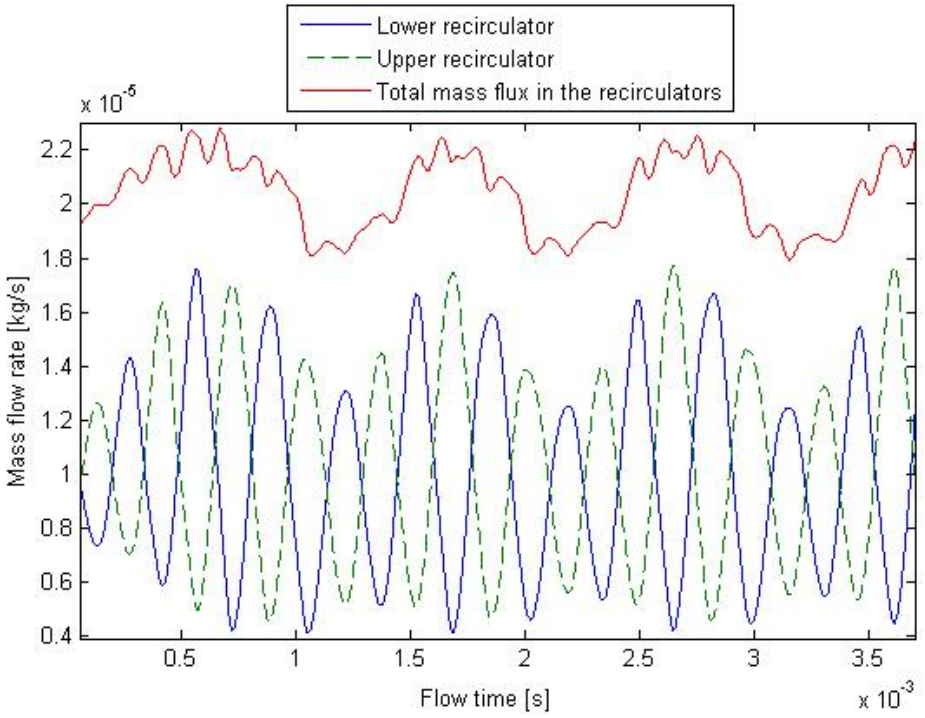

FIGURE 7.14: Total, top and lower feedback channels mass flow rate for inlet gauge pressure of 10 kPa and turbulent conditions

to identify the phase gap, figure 7.15 is provided. In this figure, the lower outlet mass flow rate and the lower feedback channel mass flow rate are represented. Vertical lines have been added for a better comprehension of the results.

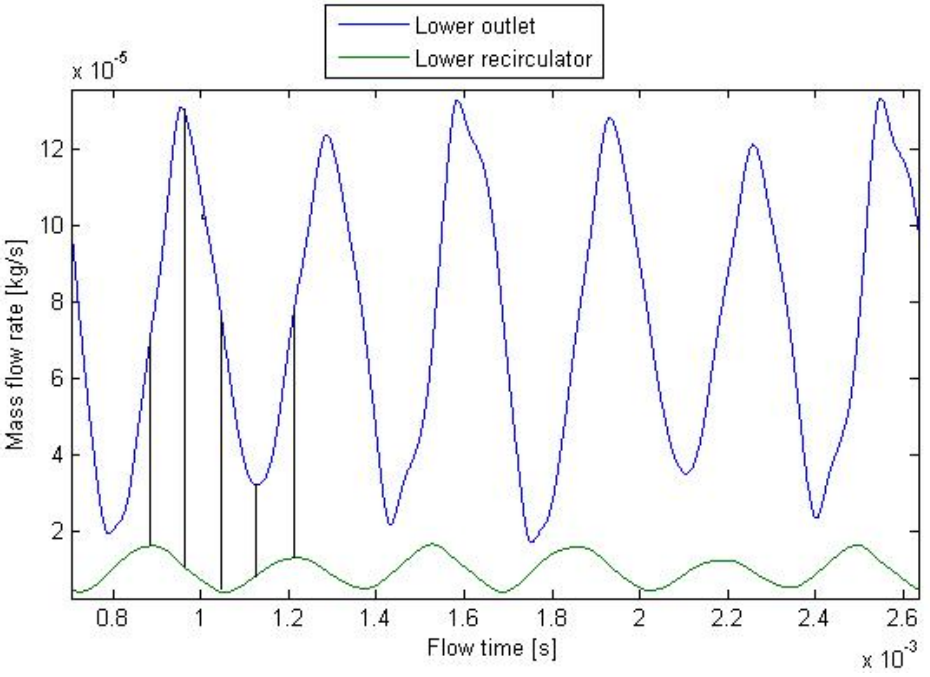

FIGURE 7.15: Lower outlet and lower feedback channel mass flow rate for inlet gauge pressure of 10 kPa and turbulent conditions

Apparently, as said before the feedback channels seem to have the same frequency as the outlet. However, the flow through the feedback channels oscillates 90 degrees before than the exiting flow. The explanation is simple if the different steps of the oscillation explained in the previous section are identified: the first vertical line in figure 7.15 represents the scenario corresponding to figure 7.8 (90 degrees); the second vertical line, represents the scenario corresponding to figure 7.9 (180 degrees); the third vertical line represents the scenario corresponding to figure 7.10 (270 degrees); and the fourth vertical line represents the scenario corresponding to figure 7.7 (0 degrees). Now, the reason for the need of the feedback channels is easily understood. As the main jet approaches the lower wall of the mixing chamber due to the Coanda effect, the lower feedback channel starts receiving the flow at its inlet. This flow is redirected to the upstream of the main jet, at the inlet of the mixing chamber. When the main jet is at its lower position the mass flux through the oscillator is still increasing. It reaches a maximum mass flux when the main jet is in the middle of the mixing chamber, being pushed upwards by the mass flux exiting from the lower feedback channel. Then, as there is no input, the mass flux through the lower feedback channel decreases until it reaches a minimum when the main jet is again in the middle of the mixing chamber but returning to the lower wall. The same process can be applied to the upper feedback channel.

In addition, it can be seen that there is always a residual mass flux in the inactive channel, but they never change their working direction. This means that while the active channel is expelling fluid, the inactive channel is also expelling fluid, but only a residual mass flux much lower than that from the active channel. Thus, the inlet of the feedback channels always suctions mass while the outlet of the feedback channels always expels mass, so the flow in the feedback channels is from the inlet to the outlet during the whole cycle.

7.3.3 Outlet backflow

As seen in figure 7.3, it is important to notice that the "inactive" outlet (the one which is not expelling the main jet) still provides a positive exiting flow, given that the mass flux is always positive. Of course it is an average mass flow for each area defined in the outlet (the top and the low halves of the outlet), so there might be small regions of the outlet where there is a slight backflow inside the oscillator. However, the global balance on the inactive outlet indicates that most part of the flow in that area is exiting. On the first place, this means that the oscillating amplitude is small, a little fraction of the main jet might even be still in the inactive outlet. Besides, it also means that there is no significant backflow current in the outlet, unlike other fluidic oscillators such as the one studied by Ruiz [8]. In fact, figure 7.16 shows the X velocity field of the oscillator and

it is clear that there is not an important backflow current in the outlet in comparison with the main jet velocity.

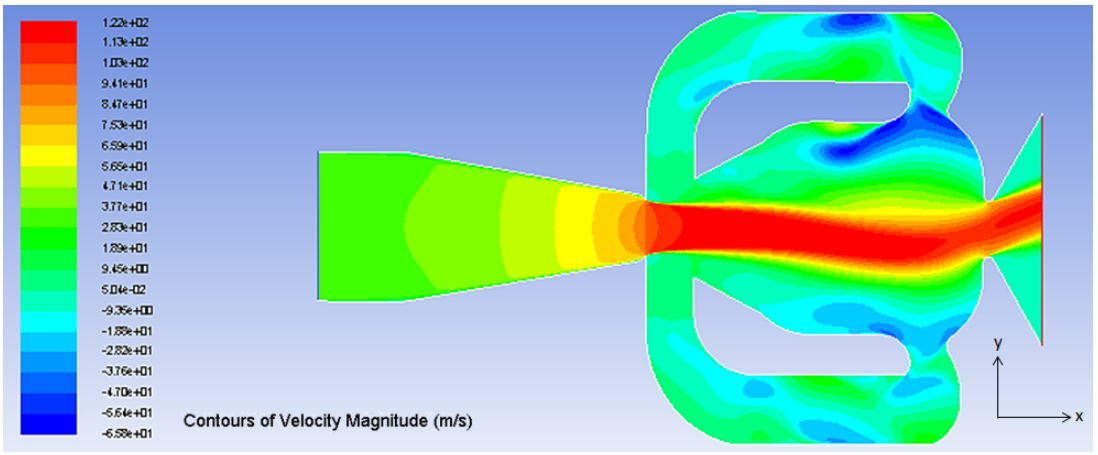

FIGURE 7.16: X velocity field for inlet gauge pressure of 10 kPa and turbulent conditions

Chapter 8

Budget

The project budget includes all the economical expenses to consider during its realization. The different expenses have been separated in the following tables so that each cost item is clearly identified. In table 8.1, the human resources needed to complete the study are detailed:

	Time dedication [hours]	€/h	Cost [€]
Planning and software learning	80	15	1200
Numerical analysis	200	15	3000
Draft preparation	100	15	1500
Total	**380**		**5700**

Table 8.1: Human resources cost.

Table 8.2 shows the computational costs dedicated to the present work. Note that the cost of the energy used by the computer has not been considered in the budget, as it is three orders of magnitude lower than the total cost.

	Units	Anual license [€]	€/h	Cost [€]
MATLAB Licence	380h	2000	1.11	422.22
ANSYS Licence	380h	24903.36	13.84	5257.38
Total				**5679.6**

Table 8.2: Computational resources cost.

Finally, the total cost of the study is **11379.60 €**.

In this work, the integration of fluidic oscillators in real applications and the manufacturing process are not studied. However, the major disadvantage of fluidic oscillators lies in the technical aspects of their integration into other systems, such as a wing, not in the economical aspects. As soon as applications are feasible, it will become a very useful device that is very likely to play an important role in transportation systems. Therefore, investing on fluidic oscillators seems an interesting option.

Chapter 9

Environmental study

The only resource used during the study has been a computer for the numerical analysis and a cluster. Given that, the whole study does not harm the environment in any way, apart from the energy consumption which is obviously negligible in this case. What is more, it might be seen as beneficial, in regards of the fact that if such study was to be made by experimental means, the usage of material, the machinery cost, the energy consumption and many other factors would entail a much more negative environmental and economical impact.

Nonetheless, the study itself is the least important factor that should be considered in an analysis of the environmental impact: the consequences of the applications of the fluidic oscillator, which are detailed in the following sections, are much more significant. In fact, the fundamental reason for investigation in fluidic oscillators is the development of an environmental friendly technology that can replace current devices.

9.1 Advantages

- Investigation in the field of jet mixing enhancement applied to combustion intends to decrease pollutant products and increase combustion efficiency, thus reducing harmful emissions and fuel consumption at the same time.
- Thrust vectoring, on the other hand, allows weight saving by reducing the amount of mass needed to deflect a jet. It has been proved that the use of a miniature fluidic oscillator of much less mass than the current technology can create the same effect [1]. By reducing the mass of an aeroplane or a rocket, for example, a lot of fuel is saved, given that the lift is reduced and thus the required velocity is also reduced.

- Boundary layer control allows a later boundary layer separation, increasing lift in an aeroplane and reducing drag considerably in all kinds of vehicles. Having a higher lift allows a lower required speed in take-off, landing, manoeuvring and in general the whole flight, reducing the required thrust and then reducing the fuel consumption as well. Less drag also implies that the required thrust is decreased and fuel consumption is reduced. In addition, stall can be also delayed to extremely steep angles, allowing higher lift and increasing the manoeuvrability of an aeroplane.

- The simple possibility of substituting the current and complex high-lift devices such as flaps with fluidic oscillators results in a lot of weight and drag reduction, with the same consequences explained above.

- Fluidic oscillators have very low requirements of mass flow rates and energy, or even no energy requirements in some cases.

- Easy manufacturing and wide range of materials availability are also an advantage, as the environmental footprint becomes minimal.

- Reliability is another important factor. The absence of moving parts and the simplicity of their design ensure a long durability and little maintenance requirements, so less spare parts and less units must be produced, which entails that the residual wastes are also reduced.

9.2 Disadvantages

- The main disadvantage nowadays is the fact that a lot of investigation is still needed in order to fully understand the working principles of the fluidic oscillator. Because of that, a lot of resources still have to be used during the investigation and development of the most efficient oscillator, while other already developed devices do not need this investment.

- Although fluidic oscillators can reduce fuel consumption and combustion emissions, it still does not provide a definitive solution for the energetic crisis.

In conclusion, the advantages clearly surpass the disadvantages, so the overall environmental impact is, without question, positive. In the near future, fluidic oscillators could set a turning point for transportation systems, increasing their efficiency and reducing their environmental impact considerably. This can lead to many other positive effects in the global economy and technology development.

Chapter 10

Conclusions

After reviewing the current available technology for aeronautical applications of the fluidic oscillators (boundary layer control and thrust vectoring), it is clear that fluidic oscillators represent a strong competitor that is likely to replace other devices. Its simplicity, low cost (operating costs, manufacturing costs and energy requirements) and low environmental impact will guarantee their use as soon as there is a deeper understanding of their working features and their integration into real systems is feasible.

The aim of this work is to compare the numerical analysis of a fluidic oscillator with the experimental analysis performed by Raghu [1]. The geometry has been reproduced and meshed, generating 3 different meshes. The mesh independence test has shown that the coarse mesh has the best balance between accuracy and time requirements for the scope of this project, so this has been the chosen mesh. However, the present results should be regarded as preliminary results that need to be validated by future studies, which could use finer meshes and provide more time to the simulations.

As for the results, it is clear that the frequencies obtained do not resemble the experimental values. The incompressibility hypothesis and the available time for the simulations have not allowed the best of results. However, a difference between the experimental and the present geometry is probably the main reason for the disagreement. Besides, the fact that the mass fluxes are slightly different from the experimental ones support this possibility. Future studies have been suggested in order to verify the present results. They should account for compressibility, set smaller time steps and increase the order of the spatial discretisation. Besides, the range of inlet pressures studied for the oscillator should be enlarged. Moreover, the third dimension could be also studied and even changes could be made to the geometry in order to try to obtain the same frequencies as in the experimental study or to study the importance of each part of the oscillator geometry in the resulting oscillation.

The dependence of the outlet flow frequency has been studied in front of the inlet velocity and it follows a linear tendency, in accordance with the conclusions in the work by Ruiz [8].

Apart from that, for a Reynolds number of 2800, the non-steady-state laminar simulation has been capable of providing an oscillatory flow. It would be interesting to continue with this analysis, studying lower Reynolds numbers. This might show that turbulence does not play such important role in the working principles of the fluidic oscillators and that in practical applications the mass flow requirements can be reduced even to the point of laminar flow, having still an oscillation.

It is important to highlight the difficulties found for convergence of the simulations. It seems that the time step used for the simulations might have been excessively high. Therefore, time steps larger than 10^{-6} s should be avoided in future works.

Finally, the flow characterisation of the oscillator has been performed, clearly identifying the significant features of the flow inside the fluidic oscillator and proving the influence of the feedback channels in the exiting flow. This study has established the preliminary background for future studies of the present fluidic oscillator that should provide more accurate data and a wider range of study.

Chapter 11

Future work

After this work, there are several other approaches that might be of interest, based on this study:

- Application of compressible flow and lower time steps to the current simulations, in order to verify the results and study of the compressible flow region for the same fluidic oscillator. The compressible flow region has not been studied here and most part of the experimental results belong there.
- Study of low Reynolds cases under laminar conditions only, in order to verify if a periodical oscillatory flow can be obtained without accounting for turbulence effects.
- In fluidic oscillators, where turbulence plays an important role, the 3-dimensional effects are usually significant and they cannot be considered in a 2D study. A 3D study could provide more accurate data.
- Changes on the geometry could be applied, with the aim of finding an optimal configuration that provides better performance for a certain application. In addition, those changes could be also aimed at finding the experimental geometry studied by Raghu et al. [1].
- Study of the integration of the fluidic oscillator in a real system, such as a wing.

These studies could make use of all the information contained in this document to continue with the analysis of the fluidic oscillator or analyse it from a different approach. Anyway, the work that must be performed for these studies is similar to the work done here. In order to provide the reader with an idea of the planning to be followed for the accomplishment of such works, the tasks' organisation shown in chapter 1 could be extrapolated to the proposed works.

Bibliography

[1] G. Raman, S. Packiarajan, G. Papadopoulos, C. Weissman, and S. Raghu. Jet thrust vectoring using a miniature fluidic oscillator. *The Aeronautical Journal*, (2835):129–138, 2001.

[2] James W. Gregory and Surya Raghu John P. Sullivan. Characterization of miniature fluidic oscillator flowfields using porous pressure sensitive paint. 2001.

[3] James W. Gregory, John P. Sullivan, and Surya Raghu. Visualization of internal jet mixing in a fluidic oscillator. *11th International Symposium on Flow Visualization*, 2004.

[4] S. Raghu. Feedback-free fluidic oscillator and method, 2001. US Patent 6,253,782.

[5] Gi-Hun Kim. A study of fluidic oscillators as an alternative pulsed vortex generating jet actuator for flow separation control. Master's thesis, University of Manchester, Faculty of Engineering and Physical Sciences, 2011.

[6] Jung-Tang Yang. Micro-fluidic oscillator having a sudden expansion region at the nozzle outlet. 2009.

[7] N. M. Morris. *An Introduction to Fluid Logic*. McGraw-Hill, 1973.

[8] Mikel Ruiz Arozarena. Estudio de osciladores fluídicos mediante mecánica de fluidos computacional. 2014.

[9] Javier Pérez-Herreras. Nuevas especies de espacios. *ARQ (Santiago)*, pages 30 – 37, 12 2012. ISSN 0717-6996.

[10] José Meseguer Ruiz and Ángel Sanz Andrés. *Aerodinámica básica*. Garceta, 2011.

[11] H. Schlichting and K. Gersten. *Boundary Layer Theory*. Springer, 2000.

[12] Bernhard C. Bobusch, Rene Woszidlo, J. M. Bergada, C. Navid Naveri, and Christian Oliver Paschereit. Experimental study of the internal flow structures inside a fluidic oscillator. *Experiments in fluids*, 12, 2013.

[13] *ANSYS FLUENT Theory Guide*, 2010.

[14] James W. Gregory, Ebenezer P. Gnanamanickam, and John P. Sullivan. Variable-Frequency Fluidic Oscillator Driven by Piezoelectric Devices. *AIAA Journal*, 2005.

[15] James W. Gregory, Surya John P. Sullivan, Raghu, and Ganesh Raman. Characterization of a microfluidic oscillator for flow control. *AIAA Journal*, 2004.

[16] G. Raman. Using controlled unsteady mass addition to enhance jet mixing. *AIAA Journal*, 1997.

[17] Manuel Sarmiento Calderó. Estudio de un oscilador fluídico mediante mecánica de fluidos computacional. 2014.

[18] M. Kadosch. *The Curved Wall Effect*. Second Cranfield Fluidics Conference, 1967.

[19] I. Reba. Applications of the coanda effect. *Scientific American*, 1966.

[20] Gerald H. Hogland. *Studies of bistable fluid devices for particle flow control*. PhD thesis, 1972.

[21] J. M. Kirshner and Silas Katz. *Design Theory of Fluidic Components*. Academic Press, INC., 1975.

[22] V. Tesar, S. Zhong, and F. Rasheed. New fluidic-oscillator concept for flow-separation control. *AIAA Journal*, 2013.

[23] H. Viets. Flip-flop jet nozzle. *AIAA Journal*, 1975.

[24] Ganesh Raman and Surya Raghu. Cavity resonance suppression using miniature fluidic oscillators. *AIAA Journal*, 2004.

[25] Eliphas W. Simoes, Rogerio Furlanc, R. E. B. Leminskia, Mário Ricardo Gongora-Rubio, Marcos Tadeu Pereira, Nilton Itiro Morimotoa, and Jorge J. Santiago Avilés. Microfluidic oscillator for gas flow control and measurement. *Elsevier*, 2004.

[26] R. B. Beale and M. T. Lawler. Development of a wall-attachment fluidic oscillator applied to volume flow metering. *Flow: Its measurement and control in science and industry*, 1974.

[27] R. D. Stouffer. Liquid oscillator device, 1985. US Patent 4,508,267.

[28] U. Gebhard, H. Hein, E. Just, and P. Ruther. Combination of a fluidic micro-oscillator and micro-actuator in liga-technique for medical application. In *Solid State Sensors and Actuators, 1997. TRANSDUCERS '97 Chicago., 1997 International Conference on*, volume 2, pages 761–764 vol.2, 1997.

[29] James W. Gregory, Hirotaka Sakaue, and John P. Sullivan. Fluidic Oscillator as a Dynamic Calibration Tool. *AIAA Journal*, 2002.

[30] James W. Gregory, Surya John P. Sullivan, Raghu, and Ganesh Raman. Characterization of the microfluidic oscillator. *AIAA Journal*, 2007.

[31] Eliphas W. Simoes, Rogerio Furlanc, and Marcos Tadeu Pereira. Numerical Analysis of a Microfluidic Oscillator Flowmeter Operating with Gases or Liquids.

[32] *ANSYS FLUENT User's Guide*, 2010.